Applied Catalysis B: Environmental 325 (2023) 122304

Contents lists available at ScienceDirect

Applied Catalysis B: Environmental

journal homepage: www.elsevier.com/locate/apcatb

Porous edge confinement: High carrier potential and low activation energy barrier synergistically boosting the efficiency of selective photocatalytic CO_2 conversion

Bin Wang [a,b,1], Xingwang Zhu [c,1], Fangcheng Huang [d], Yu Quan [a], Gaopeng Liu [a], Xiaolin Zhang [b], Fangyu Xiong [b], Chao Huang [b], Mengxia Ji [a], Huaming Li [a], Paul K. Chu [b,*], Jiexiang Xia [a,*]

[a] School of Chemistry and Chemical Engineering, Institute for Energy Research, Jiangsu University, 301 Xuefu Road, Zhenjiang 212013, China
[b] Department of Physics, Department of Materials Science and Engineering, and Department of Biomedical Engineering, City University of Hong Kong, Tat Chee Avenue, Kowloon, Hong Kong, China
[c] College of Environmental Science and Engineering, Yangzhou University, Yangzhou 225009, China
[d] Department of Information Engineering, Electronics and Telecommunications, Sapienza University of Rome, Piazzale Aldo Moro 5, 00185 Roma, Italy

ARTICLE INFO

Keywords:
BiOCl
Porous nanosheets
Photocatalytic CO_2 reduction
Edge confinement
Faceted heterojunction

ABSTRACT

Catalysts which allow directional transfer of photogenerated electrons to catalytic sites are crucial to efficient photocatalytic CO_2 reduction. Herein, 2D BiOCl porous nanosheets (BOC-PNS) are prepared by triblock polymer (F127) assisted mechanical ball milling. The main exposed plane is (001) on the BOC-PNS surface and the porous structure increases the edge (110) facet. The (001)/(110) heterojunction enhances directional migration and separation of photogenerated carriers. *In situ* Raman scattering, *in situ* Fourier transform infrared spectroscopy, 3D FDTD simulation and theoretical calculations reveal that the BOC (001) plane is enriched with directionally migrating photogenerated electrons and provides the primary active sites to bridge adsorption-activated CO_2 molecules consequently producing a smaller energy barrier for the intermediate product of *COOH. Weak CO adsorption on the BOC (001) plane further promotes CO_2 reduction. Upon exposure to simulated sunlight, the CO yield of BOC-PNS is enhanced by the rich edge confinement effect reaching 28.2 μmol g^{-1} h^{-1}, which is 2.1 and 2.8 times that of the BOC nanosheets (13.5 μmol g^{-1} h^{-1}) and nanoplates (9.9 μmol g^{-1} h^{-1}), respectively.

1. Introduction

Semiconductor-catalyzed photosynthesis is an important sustainable strategy to minimize the use of fossil energy and greenhouse effect [1,2]. However, hysteretic photogenerated carrier separation and sluggish CO_2 adsorption-activation on semiconductors are bottlenecks plaguing large-scale commercial adoption of artificial photosynthesis [3]. By adopting a two-pronged approach including directional migration and effective separation of photogenerated electrons together with effective adsorption and activation of CO_2 molecules, the photocatalytic CO_2 conversion efficiency can be enhanced [4].

Semiconductors can be prepared to expose different crystal planes [5]. For different orientations, the periodicity and density of atoms vary leading to different physical and chemical properties as well as anisotropy [6,7]. In polycrystalline semiconductors, it is difficult for photogenerated carriers to migrate directionally after light excitation and consequently, rapid electron-hole recombination occurs [8]. In addition, the crystal surface enriched by photogenerated electrons is not on the same surface as the catalytic active sites thus not facilitating catalytic reactions [9]. Therefore, how to precisely control the exposed crystal planes and plane composition is critical to achieving directional migration of photogenerated carriers to the redox reaction active sites for high-efficiency photocatalysis [10]. The lateral size of two-dimensional semiconductors is larger than the thickness and the (001) crystal plane perpendicular to the c-axis direction is normally exposed, whereas the edge exposes the (110) or ($1\bar{1}0$) planes primarily because of the small thickness [11,12]. This unique surface anisotropy of two-dimensional semiconductors can be exploited to improve

* Corresponding authors.
E-mail addresses: paul.chu@cityu.edu.hk (P.K. Chu), xjx@ujs.edu.cn (J. Xia).
[1] These authors contributed equally to this work.

https://doi.org/10.1016/j.apcatb.2022.122304
Received 1 October 2022; Received in revised form 6 December 2022; Accepted 16 December 2022
Available online 23 December 2022

directional migration and accumulation of photogenerated carriers. If the region enriched with photogenerated electrons happens to be the active CO_2 adsorption sites, the photocatalytic CO_2 conversion efficiency can be improved [6,12]. In addition, ultrathin 2D materials exhibit the unique edge confinement effects such as the quantum spin Hall effect for topological insulators [13], edge plasmon enhancement effect for black phosphorene [14], as well as strain effect caused by edge coordination unsaturation [15]. Hence, increasing the edge sites on 2D materials can enhance directional migration of photogenerated carriers and subsequent photocatalytic CO_2 conversion.

In order to confirm that multi-edge 2D semiconductors can indeed enhance photocatalytic CO_2 conversion and understand the pertinent mechanism, the two-dimensional semiconductor BiOCl has been studied. It belongs to the V-VI-VII group of multi-component metal oxyhalides with the crystal structure being the PbFCl tetragonal type. It has high chemical stability and is nontoxic as well as corrosion resistant [16]. BiOCl has a layered structure in which the $[Bi_2O_2]$ layer and double halogen layer are intertwined along the c-axis [17]. There are strong covalent bonds between the inner atoms but weak van der Waals force between layers. The crystal structure provides enough space for polarization of the related atoms and orbitals to form an internal electrostatic field along the direction perpendicular to the $[Bi_2O_2]$ and [Cl] layers, which can facilitate efficient separation of photogenerated electrons and holes [18]. However, there have been few studies on ultrathin 2D BiOCl with the multi-edge structure and the effects of the nanosheet thickness, structure, and surface defects are not well understood [19]. In order to increase the edge sites on 2D BiOCl, ultrathin 2D porous BiOCl nanosheets can be prepared with a high yield by the milling-assisted soft template method. Compared with the traditional solvothermal method such as the hard template method and high temperature calcination, the ball milling-assisted soft template method is faster as well as more controllable, environmentally friendly, and energy saving boding well for commercialization.

Herein, 2D BiOCl porous nanosheets (BOC-PNS) are produced by the ball milling-assisted soft template (F127) method (Fig. 1a). Mesopores are uniformly distributed in the BiOCl nanosheets to enhance the edge structure. The primary exposed face of BOC-PNS is (001) and the edge exposes the (110) plane. The (001)/(110) heterostructure provides high-speed channels for directional migration and separation of photogenerated carriers. The (001) facet constitutes the enriched sites for

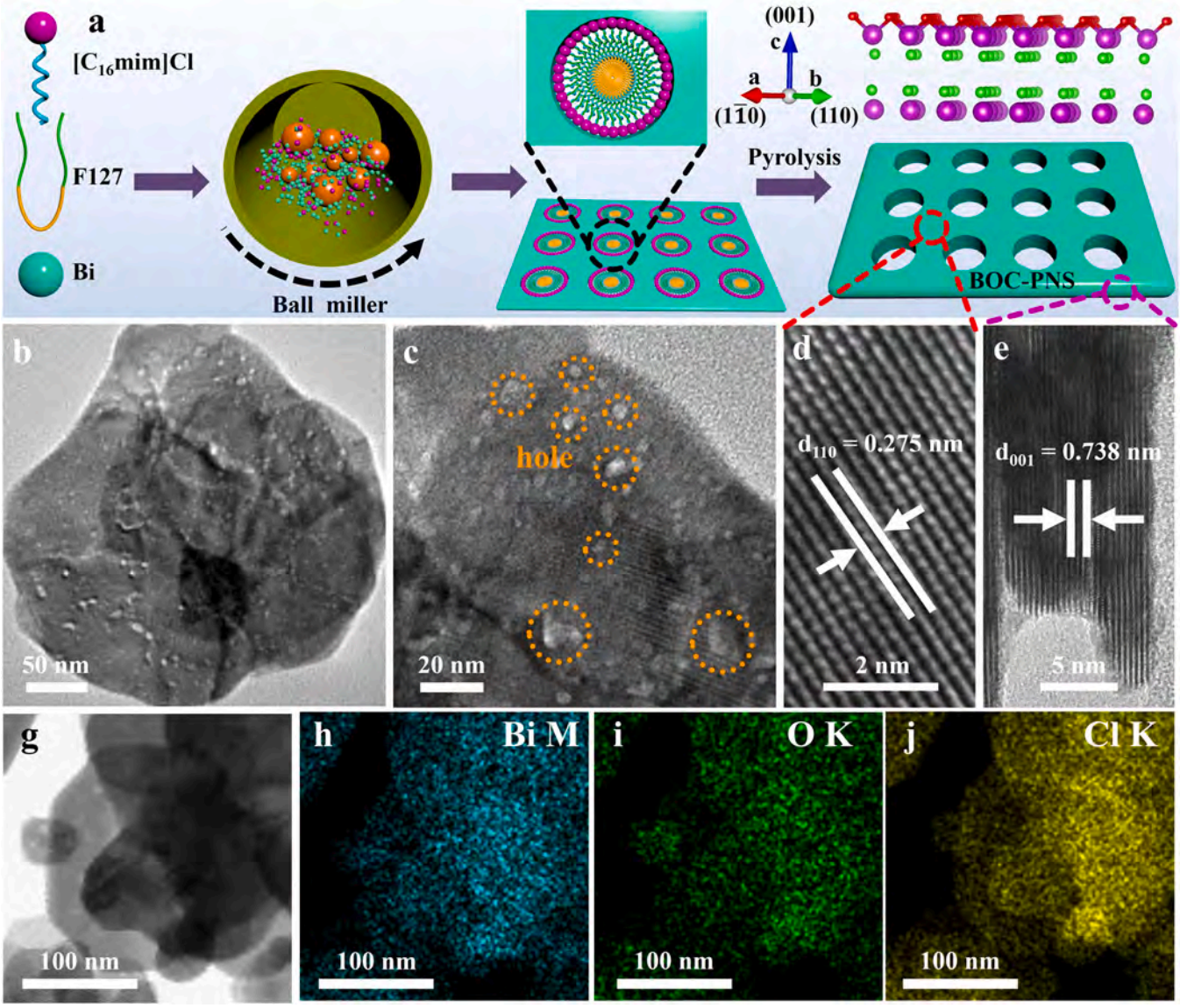

Fig. 1. (a) Schematic showing the synthesis of BOC-PNS. (b, c) TEM and (d, e) HR-TEM images of BOC-PNS. (g-j) TEM image and corresponding elemental maps of BOC-PNS.

photogenerated electrons and also the main active sites for adsorption and activation of CO_2. CO_2 molecules are activated by bridging adsorption on the (001) plane and the conversion energy barrier of the intermediate product *COOH decreases. In the 2D porous edge-rich BOC nanosheets, directional migration of photogenerated electrons and enrichment of the (001) plane active sites synergistically boost the efficiency of CO_2 reduction. Upon illumination with simulated sunlight, the CO yield of BOC-PNS is 28.2 μmol g^{-1} h^{-1}, which is 2.1 and 2.8 times that of the BiOCl nanosheets (BOC-NS, 13.5 μmol g^{-1} h^{-1}) and BiOCl nanoplates (BOC-NP, 9.9 μmol g^{-1} h^{-1}), respectively. The results reveal a novel and effective strategy to improve the photocatalytic efficiency in artificial photosynthesis.

2. Experimental section

2.1. Materials and chemicals

$Bi(NO_3)_3{\cdot}5H_2O$ (AR, ≥ 99.0%) and KCl (AR, ≥ 99.0%) were obtained from Sinopharm Chemical Reagent Co., Ltd. Triblock copolymer Pluronic F127 (M_w =12600, $PEO_{106}PPO_{70}PEO_{106}$) was purchased from Aldrich Corp. and $[C_{16}mim]Cl$ was provided by Lanzhou Greenchem ILS, LICP, CAS, China. All the regents were used without purification.

2.2. Materials fabrication

2.2.1. Preparation of BOC-PNS

The schematic diagram of the synthesis of BOC-PNS is shown in Fig. 1a. Briefly, 1 mmol $Bi(NO_3)_3{\cdot}5\ H_2O$, 1 mmol $[C_{16}mim]Cl$ ionic liquid, and 0.5 g of F127 were added to the agate ball-milling jar and ground using the planetary ball mill for 1 h. The solid mixture was collected, washed several times with deionized water and ethanol, and dried in a vacuum oven at 60 °C for 12 h. The solid product was then calcined at 400 °C in air for 2 h in a tube furnace to obtain BOC-PNS.

2.2.2. Preparation of BOC-NS

1 mmol $Bi(NO_3)_3{\cdot}5\ H_2O$ and 1 mmol $[C_{16}mim]Cl$ ionic liquid were added to the agate ball-milling jar and ground using the planetary ball mill for 1 h. The solid mixture was collected, washed with deionized water and ethanol several times, and dried in a 60 °C oven for 12 h. The solid product was calcined at 400 °C in a tube furnace for 2 h under ambient conditions to obtain BiOCl-NS.

2.2.3. Preparation of BOC-NP

1 mmol $Bi(NO_3)_3{\cdot}5\ H_2O$ and 1 mmol KCl were added to a beaker containing 20 mL of deionized water. The mixture was dispersed ultrasonically and stirred for 5 h. The product was collected by centrifugation, rinsed several times with deionized water and ethanol, dried in 60 °C oven for 12 h, and calcined at the temperature of 600 °C in air in a furnace for 2 h to obtain BiOCl-NP.

2.3. Characterization

The powder X-ray diffraction (XRD) patterns were acquired by the XRD-6100 (Shimadzu) and the Raman scattering spectra were obtained on the micro-Raman spectrometer (Renishaw Invia) with a back-scattering geometry and 532 nm laser. The specific surface area and particle size were determined by the Brunauer-Emmett-Teller (BET) method based on the N_2 adsorption-desorption isotherms (Micromeritics Instrument Corporation, USA). Fourier transform infrared (FTIR, Nexus 470, Thermo Electron Corporation) was carried out using the standard KBr disk method. UV–vis spectrophotometry and X-ray photoelectron spectroscopy (XPS) were performed on the UV-2450 spectrophotometer (Shimadzu) and PHI5300 with a monochromatic Mg K_α source, respectively. The morphology and structure were examined by scanning electron microscopy (SEM) (JEOL JSM-7001 F) and transmission electron microscopy (TEM) (JEOL-JEM-2010). Photoluminescence (PL) was performed on the Varian Cary Eclipse spectrometer. The photocurrents, Mott-Schottky plots, and electrochemical impedance spectroscopy (EIS) date were obtained from the phosphate buffer solution (0.1 M PBS, pH = 7.0), 0.1 M KCl, and 0.1 M KCl containing 5 mM $Fe(CN)_6^{3-}/Fe(CN)_6^{4-}$, respectively on the CHI 760E electrochemical system (CH Instruments Ins.). The *in situ* FT-IR spectra were acquired by *in situ* diffuse reflectance infrared Fourier transform infrared spectroscopy (Thermo fisher Nicolet iZ10, USA). The catalyst surface was first cleaned with He at 120 °C and after cooling to room temperature, the background was measured and CO_2 and water vapor were introduced in the dark. The adsorption/desorption equilibrium between the catalyst and reactants is maintained for a period of time and FTIR spectra were collected at different time to monitor the process.

2.4. Three-dimensional finite-difference time-domain (FDTD) simulation

The light-induced semiconductor electric field strength of BOC-PNS was simulated by the FDTD method (Lumerical Solutions, v.8.11.387). The model of BOC-PNS was determined based on the TEM photographs of BOC-PNS. The BOC-PNS model consists of nanosheets with a length of 200 nm and thickness of 5 nm in a uniform porous structure. A plane wave with a broad wavelength range from 300 to 800 nm was used for normal incidence and the polarization direction of the light excitation was parallel to the x axis. The optical constants of BOC were adopted from the values proposed by the Vienna *ab initio* Simulation Package (VASP 5.4) code. The size of the boundary was divided with the x, y axis being the 2 nm meshes and z axis being the 0.2 nm meshes.

2.5. Density functional theory (DFT) computation

The density functional theory (DFT) calculation is carried out in Vienna *ab initio* simulation package (VASP). A spin polarized GGA PBE functional [20], an all-electron plane wave basis set with an energy cutoff of 520 eV, and a projection enhanced wave (PAW) method [21, 22] were used. Use p (2 × 2) BiOCl is simulated by the surface model of unit cell periodicity. Use (3 × 3 × 1) Monkhorst Pack grid samples Brillouin zone integration. The conjugate gradient algorithm is used for optimization. The convergence threshold is set to the total energy of $1 * 10^{-4}$ eV and the force of 0.05 eV/Å on each atom.

Change of adsorption energy (ΔE_{abs}) is determined as follows:

$$\Delta E_{abs} = E_{total} - E_{sur} - E_{mol}$$

E_{total}: total energy for the adsorption state, E_{sur}: energy of pure surface, E_{mol}: energy of substrate.

Free energy change (ΔG) for adsorptions is determined as follows:

$$\Delta G = E_{total} - E_{sur} - E_{mol} + \Delta E_{ZPE} - T\Delta S$$

ΔE_{ZPE}: zero-point energy change, ΔS: entropy change.

2.6. Photocatalytic CO_2 reduction activity

30 mg of the photocatalyst and 1 mL of H_2O were added to a reactor made of quartz glass (Labsolar-6A, Beijing Perfectlight Technology Co., Ltd.) and 99.99% CO_2 was used in the assessment. Photocatalytic CO_2 reduction proceeded by illuminating with a 300 W Xe lamp (PLS-SXE300D, Beijing Perfectlight Technology Co., Ltd.) and the temperature was controlled to be 5 °C by a thermostatic water bath. The gaseous products were analyzed by gas chromatography (Zhejiang FuLi Chromatograph Instruments Co., Ltd. GC9790II with the flame ionization detector (FID), thermal conductivity detector (TCD), and capillary column).

3. Results and discussion

3.1. Preparation and characterization of BiOCl

Fig. 1a illustrates the preparation BOC-PNS. During ball milling, the triblock polymer F127 self-assembles with the ionic liquid [C_{16}mim]Cl *via* hydrogen bonding. After reacting with Bi^{3+}, the self-assembled organic long chains preserve the hole on the BOC nanosheets. The 2D porous BOC-PNS is prepared by calcination at 400 °C for two hours in air. Compared to the traditional hard template and etching methods, the soft template method assisted by ball milling is more efficient, environmentally friendly, and energy saving meeting the requirements for commercial production [23]. The TEM images reveal that the plane size of the prepared BOC-PNS is about 200 nm (Fig. 1b) and there are abundant pores with a diameter of about 10 nm (Fig. 1c). HR-TEM discloses lattice fringes of 0.275 nm for the BOC-PNS plane (Fig. 1d), which belongs to the (110) plane of BOC [7,24]. The lattice spacing at the edge is about 0.738 nm (Fig. 1e) stemming from the (001) plane of BOC [25]. Growth of BOC-PNS along the c-axis direction is suppressed. The (001) crystal plane of the nanosheet is exposed primarily, but the side exposes the (110) plane. The edge thickness is about 5 nm. The EDS maps (Fig. 1g-j) reveal well dispersed Bi, O, and Cl. Compared to BOC-PNS without addition of the triblock polymer F127, BOC-NS without the porous structure on the flat surface is composed of 2D nanosheets 200 nm in width (Fig. S1a-b). To compare the physicochemical and catalytic properties with those of BOC-PNS and BOC-NS, bulk BOC-NP is prepared by conventional calcination (Figs. S1c-d).

Fig. 2a shows that the XRD peaks from BOC-PNS, BOC-NS, and BOC-NP match the BiOCl standard card JCPDS No. 06–0249 without impurities indicating that pure BiOCl is produced. The thickness decreases in the order of BOC-NP to BOC-NS to BOC-PNS and the edge effects of the porous structure accentuate. The XRD diffraction peaks shift gradually to lower angles (right side of Fig. 2a). As shown in the Raman scattering spectra (Fig. 2b), the peaks at 61.2, 144.3, and 201.0 cm^{-1} correspond to the Bi-Cl stretching modes of outer A_{1g}, inner A_{1g}, and inner E_g, respectively, and that at 398.8 cm^{-1} belongs to E_g and B_{1g} due to the movement of oxygen atoms [26]. The Raman peaks also shift gradually to smaller wavenumbers and the peak intensity decreases on account of the enhanced edge phonon confinement effect of the BOC nanosheets [27]. The nitrogen adsorption and desorption curves show that the BET

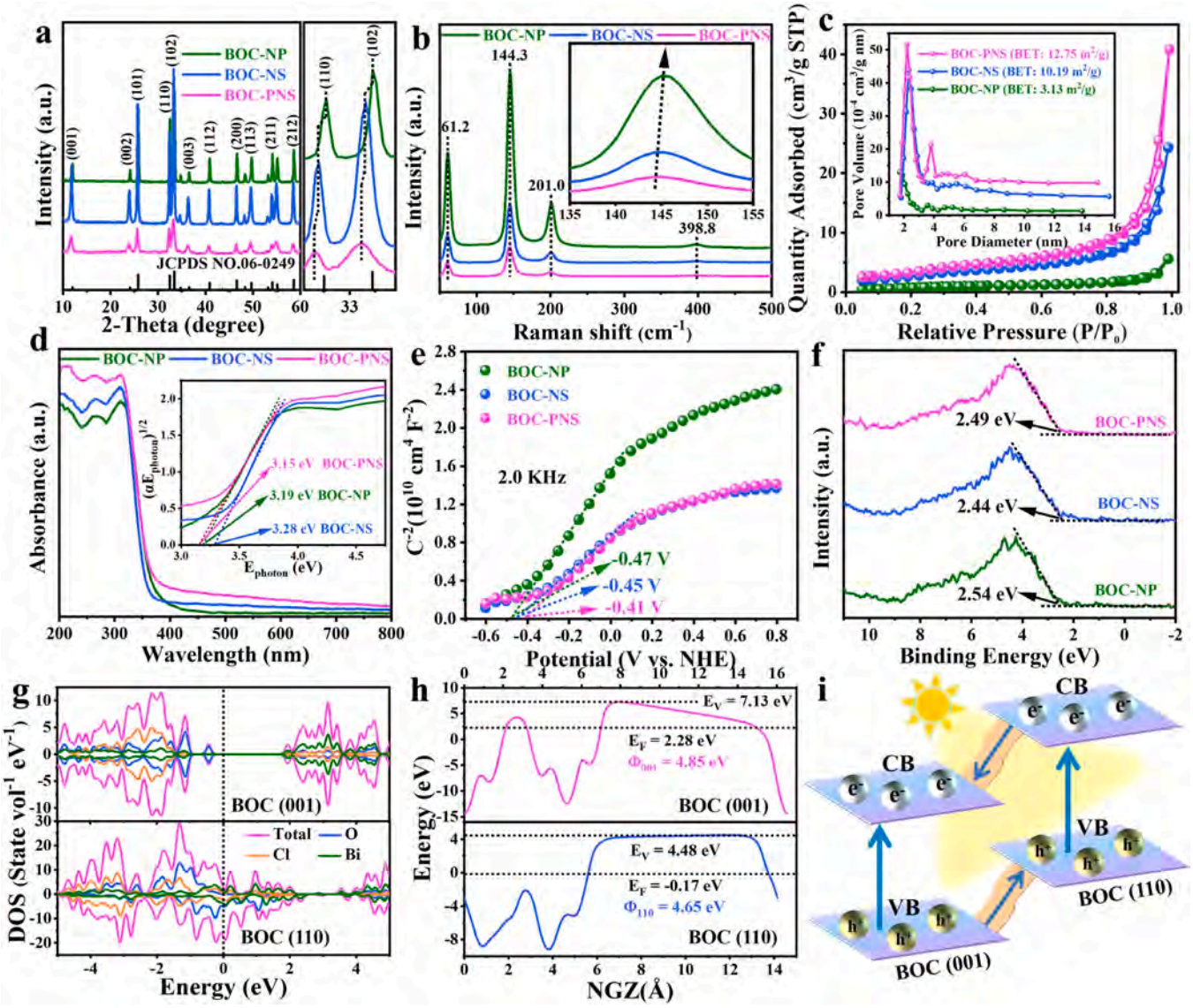

Fig. 2. (a) XRD patterns, (b) Raman scattering spectra, (c) Nitrogen adsorption-desorption isotherms (inset: pore size distributions), (d) UV-Vis diffuse reflection spectra (inset: $(\alpha E_{photon})^{1/2}$ *vs* E_{photon} curves), (e) Mott-Schottky plots, and (f) XPS valence band spectra of BOC-PNS, BOC-NS and BOC-NP. (g) Calculated density of states and (h) Work functions of BOC (001) and BOC (110). (i) Schematic diagram illustrating charge migration between the BOC (001) and BOC (110) facets.

specific surface areas of BOC-PNS, BOC-NS, and BOC-NP are 12.75, 10.19, and 3.13 m^2 g^{-1}, respectively (Fig. 2c). The 2D layered and porous structure increases the specific surface area. The pore size distribution of BOC is determined by the Barrett-Joyner-Halenda (BJH) method (Fig. 2c inset). Compared to BOC-NP and BOC-NS, BOC-PNS has more pores. Materials with a larger specific surface area and porous structure expose more active sites and are expected to adsorb more reactants (CO_2) for improved photocatalytic CO_2 reduction [28]. The optical absorption properties and band gaps are investigated by UV-Vis diffuse reflectance spectroscopy. As shown in Fig. 2d, the absorption edge of all the BOC samples is about 350 nm, but the light absorption ability of BOC-PNS is stronger than that of BOC-NP and BOC-NS. The $(\alpha E_{photon})^{1/2}$ *vs.* E_{photon} curves of BOC-NP and BOC-NS are obtained and BOC-PNS is analyzed by the classical Tauc method. The bandgaps are determined to be 3.19, 3.28, and 3.15 eV, respectively (Fig. 2d **inset**).

According to the Mott-Schotty curves (Fig. 2e), the slope of BOC is positive at 2.0 kHz revealing that BOC is an *n*-type semiconductor. By extrapolating the X-intercept in the Mott-Schottky curve, the flat-band potentials of BOC-NP, BOC-NS, and BOC-PNS are −0.47, −0.45, and −0.41 V *vs.* NHE (pH = 7), respectively. For an *n*-type semiconductor, the Fermi level is approximately the flat-band potential [29]. By considering the XPS-VB results (Fig. 2f) and Mott-Schottky curves, the VB values of BOC-NP, BOC-NS, and BOC-PNS are 2.07 V, 1.99 V and 2.08 V, respectively. According to the formula: $E_{CB} = E_{VB} - E_g$, the conduction band values of BOC-NP, BOC-NS, and BOC-PNS are −1.12, −1.29 and −1.07 V, respectively. The band structure of BOC is depicted in Fig. S3. HR-TEM shows that BOC exposes the (001) and (110) planes. Density-functional theory (DFT) calculation is performed to derive the density of states and work function. The BOC (001) plane has lower CB and VB than those of the (110) plane and the work function of the (110) plane is smaller than that of the (001) plane (Fig. 2g-h and S4). Therefore, during light irradiation, photogenerated electrons will accumulate at the (001) crystal plane, while holes will move along the (110) plane (Fig. 2i) [30]. Directional migration of photogenerated carriers facilitates separation of electrons and holes for the redox reactions.

3.2. *Photoelectrochemical properties and photocatalytic CO_2 reduction of BiOCl*

The photogenerated carrier migration and separation efficiency are assessed by electrochemical impedance spectroscopy, transient photocurrents, and fluorescence spectroscopy. As shown in Fig. 3a, the diameters of Nyquist semicircles of BOC-NP, BOC-NS, and BOC-PNS diminish gradually, indicating that the two-dimensional nanosheets and porous structure reduce the resistance against electron transfer and increase the migration speed of photogenerated electron [31,32]. All the BOC samples show photocurrent responses under irradiation and good response is observed in the multiple switching lamp cycling test (Fig. 3b). BOC-PNS exhibits the largest current after irradiation of about 2–3 times that of the BOC-NP and BOC-NS. The large photocurrent indicates high photogenerated carrier separation efficiency [33,34]. Photoluminescence is performed to investigate the efficiency of carrier separation (Fig. S5) and emission from BOC-PNS is the lowest but that from BOC-NP is the highest. Weak photoluminescence reflects low recombination efficiency of photogenerated carriers [35,36]. Time-resolved transient fluorescence confirms that BOC-PNS has the longest photogenerated electron lifetime which increases the probability of the charge participation in the photocatalytic reaction (Fig. 3c) [36, 37]. All in all, BOC-PNS with the abundant (001)/(110) facet is demonstrated to have high carrier separation efficiency.

The photocatalytic CO_2 reduction efficiency of the BOC materials is evaluated without cocatalysts and sacrificial agents. A 300 W Xe lamp is used as the light source and 5 °C water is circulated to maintain the temperature of the system. After illumination for 5 h, the products and yield are determined by gas chromatography. There are no hydrogen and hydrocarbon products in the gas and no dissolved products in the aqueous solution. Only CO gas can be detected. The CO yield of BOC-PNS is 28.2 μmol h^{-1} g^{-1}, which are 2.1 and 2.8 times that of BOC-NS (13.5 μmol h^{-1} g^{-1}) and BOC-NP (9.9 μmol h^{-1} g^{-1}), respectively (Fig. 3d-e). The performance exceeds that of many bismuth-based photocatalysts reported in the literature (Table S1). Moreover, $^{13}CO_2$ and

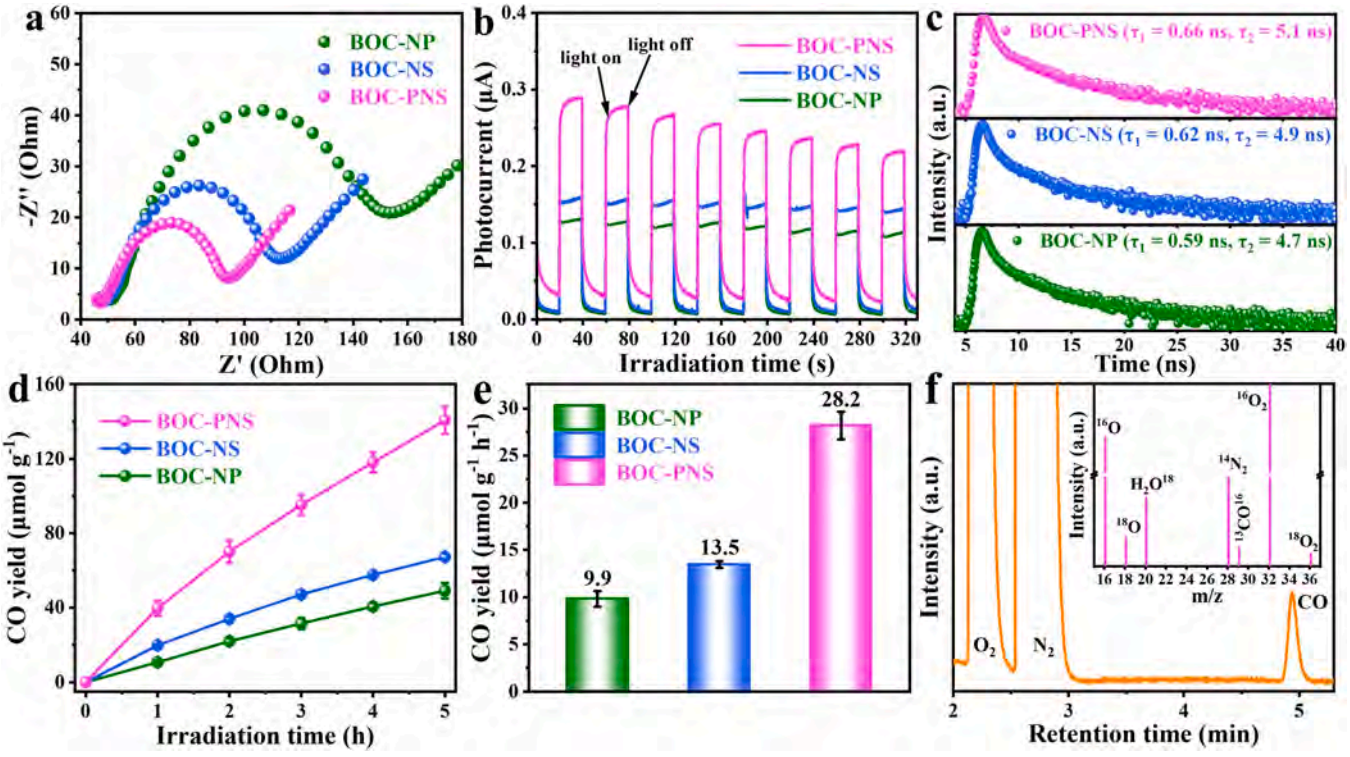

Fig. 3. (a) EIS spectra, (b) Transient photocurrent spectra, (c) Time-resolved transient PL decay curves, (d) Photocatalytic CO evolution with time, (e) CO production rates for three hours under Xe lamp irradiation for BOC-PNS, BOC-NS and BOC-NP, and (f) Mass spectra of ^{13}CO ($m/z = 29$) and $^{18}O_2$ produced on BOC-PNS.

H_2O^{18} isotope labeling experiments verify the carbon source of generated CO and the role of photogenerated holes, respectively (Fig. 3f). The peaks at $m/z = 29$ and 36 in the mass spectra can be assigned to ^{13}CO and $^{18}O_2$, respectively, indicating that CO_2 is indeed the carbon source of the generated CO and the photogenerated holes oxidize water to produce oxygen. The stretching peaks of the organic functional groups in the pristine materials do not appear from the infrared spectra of the BOC samples (Fig. S6), thus eliminating the possibility of photocatalytic decomposition of organic species on the catalysts to generate CO. Fig. S7 shows the activity diagram of BOC-PNS under continuous irradiation for 32 h. The photocatalytic activity of BOC-PNS confirms the superior characteristics during long illumination as well as stability. BOC-PNS is analyzed by XRD and SEM after the stability test (Figs. S8–9) and the structure and morphology do not change significantly.

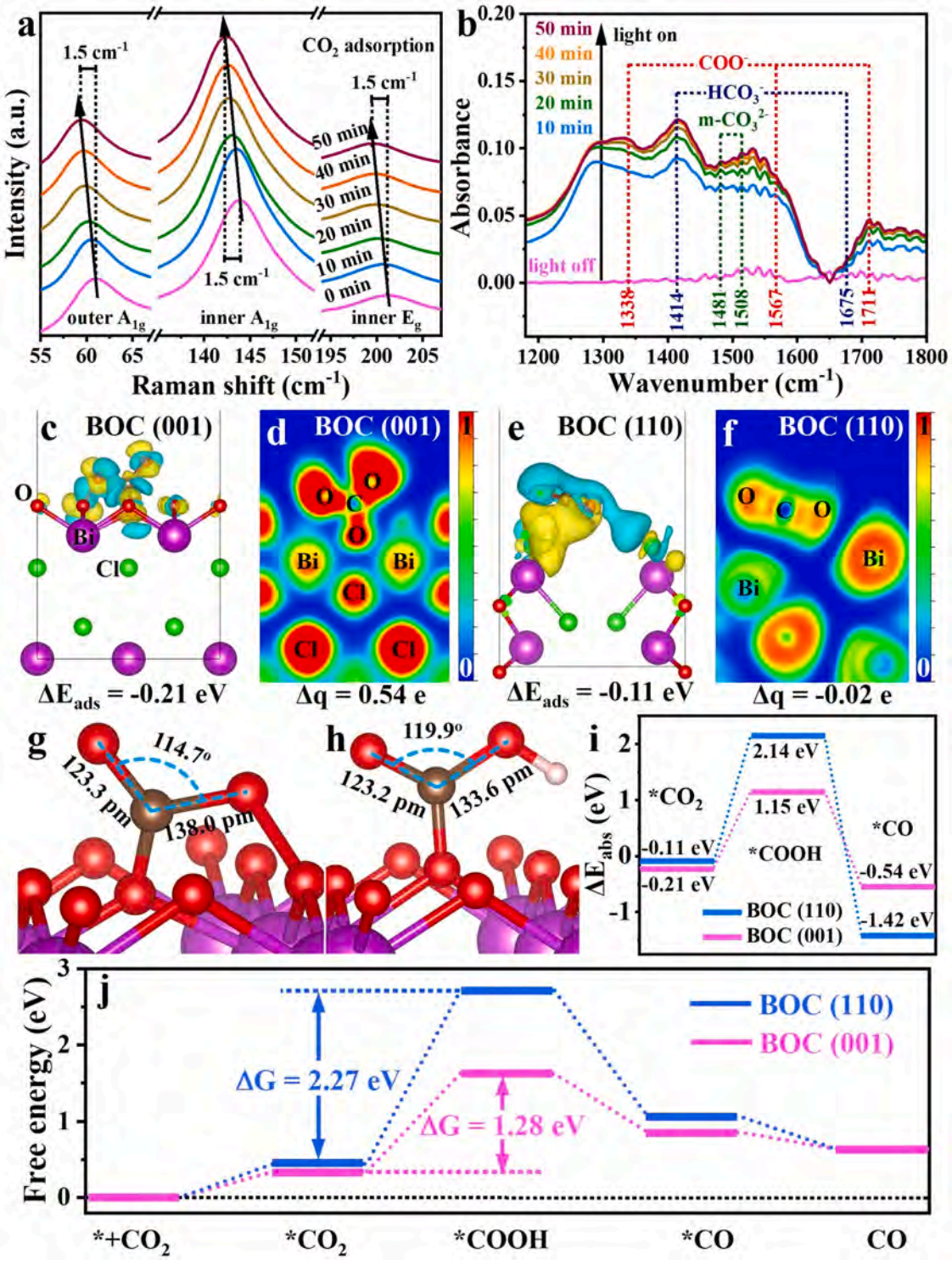

Fig. 4. (a) *In situ* Raman spectra of BOC-PNS for CO_2 reduction adsorption. (b) *In situ* FTIR spectra of BOC-PNS for simulated solar-driven CO_2 reduction. Charge difference of CO_2 adsorbed on (c, d) BOC (001) and (e, f) BOC (110). The yellow and blue regions indicate electron accumulation and depletion, respectively and Δq stands for the total charge of CO_2. Adsorption states of (g) $*CO_2$ and (h) *COOH on the surface of BOC (001). (i) Adsorption energy of $*CO_2$, *COOH and *CO on the surface of BOC (001) and BOC (110). (j) Free energy diagrams of CO_2 photoreduction to CO on BOC (001) and BOC (110).

3.3. Enhanced photocatalytic CO_2 reduction mechanism of BOC-PNS

In order to gain insights into the intrinsic mechanism responsible for the enhanced photocatalytic CO_2 reduction activity of BOC-PNS, *in situ* Raman scattering, *in situ* FT-IR and theoretical calculation are conducted. The analysis requires placing the sample in a cell *in situ*, bubbling CO_2, and testing at different time. As shown in Fig. 4a, as CO_2 is injected into the cell, the Raman peaks for the Bi-Cl stretching modes of outer A_{1g} (61.2 cm^{-1}), inner A_{1g} (144.3 cm^{-1}), and inner E_g (201.0 cm^{-1}) shift to the lower wavenumbers. According to the crystal structure of BiOCl, the outer layer of BiOCl (001) or (110) is composed of alternating Bi-O bonds (Fig. 4c-f). Hence, more CO_2 molecules are adsorbed by Bi or O in the outer layer of BiOCl leading to weakening of the Bi-Cl bond and the redshift of the Bi-Cl peak [38]. In the *in situ* FTIR analysis, BOC-PNS is first treated in helium at 120 °C to remove impurities adsorbed on the catalyst surface. After the temperature drops to room temperature, CO_2 and water vapor are introduced and BOC-PNS reaches CO_2 adsorption-desorption equilibrium after half an hour under dark conditions. Afterwards, the light is turned on to record the FTIR spectra at different time (Fig. S10a). As shown in Fig. 4**b**, the absorption peaks of monodentate carbonate (m-CO_3^{2-}) are at 1481 and 1508 cm^{-1} and those of bicarbonate (HCO_3^-) appear at 1414 and 1675 cm^{-1}. The peaks at 1338, 1567, and 1711 cm^{-1} are from COO^-. As the irradiation time is increased from 10 to 50 min, the peak intensity increases gradually [27,39]. According to previous reports, the intermediate *COOH is the rate limiting step in photocatalytic reduction of CO_2 to CO [40]. *COOH can be produced as the product CO after further protonation hydro-dehydration and the peaks at 2059 and 2077 cm^{-1} are the adsorption peaks of CO (Fig. S10b) [41,42]. As the photoreduction reaction proceeds, the peak intensity of CO increases. As shown in Fig. S10c, the peaks at 2826, 2863, 2884, 2942, and 2968 cm^{-1} are stretching (ν(CH)) modes of *HCOOH [43,44]. *HCOOH is considered an intermediate product of formic acid or hydrocarbons. In this system, photocatalytic CO_2 conversion is carried out in a gas (CO_2 +H_2O)-solid (catalyst) reaction system. Only CO is detected from the gaseous products and no formic acid or hydrocarbon products are observed. Therefore, a small amount of *HCOOH is generated to adsorb onto the catalyst surface during photocatalytic CO_2 conversion. Moreover, the four peaks in the range of 3500–3800 cm^{-1} represent -OH groups of adsorbed H_2O* (Fig. S10d) [45,46].

The mechanism of adsorption-activation of CO_2 is further studied by theoretical simulation (Table S2, Fig. 4c-g). As shown in Fig. 4c-f, CO_2 shows bridged adsorption on the BOC (001) plane. The C atom and one of the O atoms in the CO_2 molecule adsorb on two O atoms on the surface of the BOC (001) plane (-Bi-O···C-O···O-Bi-). The adsorption energy of CO_2 bridged adsorption is about − 0.21 eV. Compared to the original CO_2 molecule with a bond length 116 pm and bond angle 180°, the C-O bond length of bridged adsorbed CO_2 increases to 138.0 pm. The other bond length increases to 123.3 pm and the bond angle decreases to 114.7° (Fig. 4 g). The charge difference of CO_2 adsorbed on BOC (001) reveals that electrons of Bi-O in BOC are injected into CO_2, making the adsorbed *CO_2 molecules are electron rich (Fig. 4c-d). On the BOC (110) plane, the C atom in CO_2 is adsorbed by Bi atoms on the surface of BOC (110). The bond length (117.7 pm) and bond angle (178.6°) of CO_2 adsorbed on a single site (-O-Bi···CO_2) do not change much and the charge difference of single-site adsorbed CO_2 molecules is much smaller than that of bridge-adsorbed CO_2 (Fig. 4e-f). Hence, CO_2 can better adsorb and be activated on the BOC (001) plane for further hydrogenation and reduction. On the BOC (001) plane, the adsorbed O atom of CO_2 gains electrons and hydrogenates to form *COOH (Fig. 4 h). Fig. 4**i** shows the adsorption energies of *CO_2, *COOH and *CO on the BOC (001) and BOC (110) planes. Compared with BOC (110) ($\triangle E_{abs(*CO2)}$ = −0.11 eV, $\triangle E_{abs(*COOH)}$ = −2.14 eV, $\triangle E_{abs(*CO)}$ = −1.42 eV), BOC (001) has a stronger adsorption capacity for *CO_2 ($\triangle E_{abs(*CO2)}$ = −0.21 eV) and *COOH ($\triangle E_{abs(*COOH)}$ = 1.15 eV) but weaker adsorption capacity for *CO ($\triangle E_{abs(*CO)}$ = −0.54 eV). This indicates that the BOC (001) plane has the stronger ability to adsorb-activate CO_2 and intermediate *COOH, so that it is easier to desorb CO products. Theoretical calculation for the free energy of CO_2 reduction reveals that the intermediate product *COOH is the rate determining step in CO_2 reduction (Fig. 4j). The highest reaction energy barriers on BOC (001) and BOC (110) are 1.28 and 2.27 eV, respectively. The reaction energy barrier of CO_2 to CO conversion on BOC (001) is significantly lower than that on BOC (110). Consequently, the porous structure of BOC-PNS mainly exposes (001) planes and delivers better higher CO_2 reduction performance.

To better understand directional movement of photogenerated electrons and amplified electric field effects induced by the edges of the 2D BOC nanosheets, three-dimensional finite-difference time-domain (3D-FDTD) simulation is performed [47,48]. Nanosheets with length/-width of 200 nm and thickness of 5 nm and nanosheets of the same size with a porous structure are analyzed in the models of BOC-NS and BOC-PNS, respectively. Under irradiation with visible light (λ = 420 nm) and ultraviolet light (λ = 350 nm), the photogenerated electrons of BOC-NS migrate and accumulate mainly at the edges of the nanosheets (red region) (Fig. 5a-b), whereas the photogenerated electrons of BOC-PNS migrate efficiently both in the porous structure and at the edge (Fig. 5c-d) and the electric field vector clearly confirms the phenomenon as a result of the edge confinement effect (Fig. 5**e-h**). The 3D-FDTD simulation results reveal high-speed channels for directional migration and separation of photogenerated carriers at the BiOCl (001)/(110) heterojunction. Accordingly, the possible photocatalytic mechanism is proposed for BOC-PNS (Fig. 5**i**). When BOC-PNS is excited by light, since the conduction band and work function of BOC (001) are lower than those of the BOC (110) plane, the photogenerated electrons tend to migrate to the BOC (001) plane. The O atoms on the BOC (001) plane bridge the CO_2 molecules (-Bi-O···C-O···O-Bi-). The non-covalent bond formed by O in CO_2 and O on the surface of BOC (001) acts as a bridge to transfer the photogenerated electrons to the O of CO_2 molecule and simultaneously hydrogenates to form *COOH, which is further hydrogenated and reduced to generate CO and H_2O. BOC-PNS with porous edge confinement has high-efficiency carrier-directed transportation channels in the facet-rich heterojunction and the main exposed (001) facet weakens the CO_2 activation energy barrier to synergistically boost the efficiency of photocatalytic CO_2 conversion to CO.

4. Conclusion

Two-dimensional porous BOC-PNS materials are prepared by the triblock copolymer F127 assisted mechanical ball milling method. The 2D porous BOC-PNS with the rich (001)/(110) facet promotes separation of photogenerated electrons that gather at the porous and nanosheet edges. The BOC (001) plane provides the primary CO_2 adsorption-activation sites and reduces the energy barrier of the rate determining intermediate *COOH. Efficient desorption of the product CO on the BOC (001) plane further spurs the progress of CO_2 conversion. Owing to these advantages, BOC-PNS with porous edge confinement effect has a carrier directional migration potential and low activation energy barrier, which synergistically promote the efficiency of selective photocatalytic CO_2 conversion. The CO yield of BOC-PNS is 28.2 μmol h^{-1} g^{-1}, which is 2.1 and 2.8 times that of BOC-NS (13.5 μmol h^{-1} g^{-1}) and BOC-NP (9.9 μmol h^{-1} g^{-1}), respectively and surpasses that of many other semiconducting catalysts. The results reveal the novel concept of edge-localized catalysts and impart information about directional carrier migration and rich active sites, which are important to the design of future high-performance catalysts.

CRediT authorship contribution statement

Bin Wang: Conceptualization, Data curation, Investigation, Writing – original draft. **Xingwang Zhu:** Data curation, Investigation, Writing – original draft. **Fangcheng Huang:** Data curation, Investigation. **Yu**

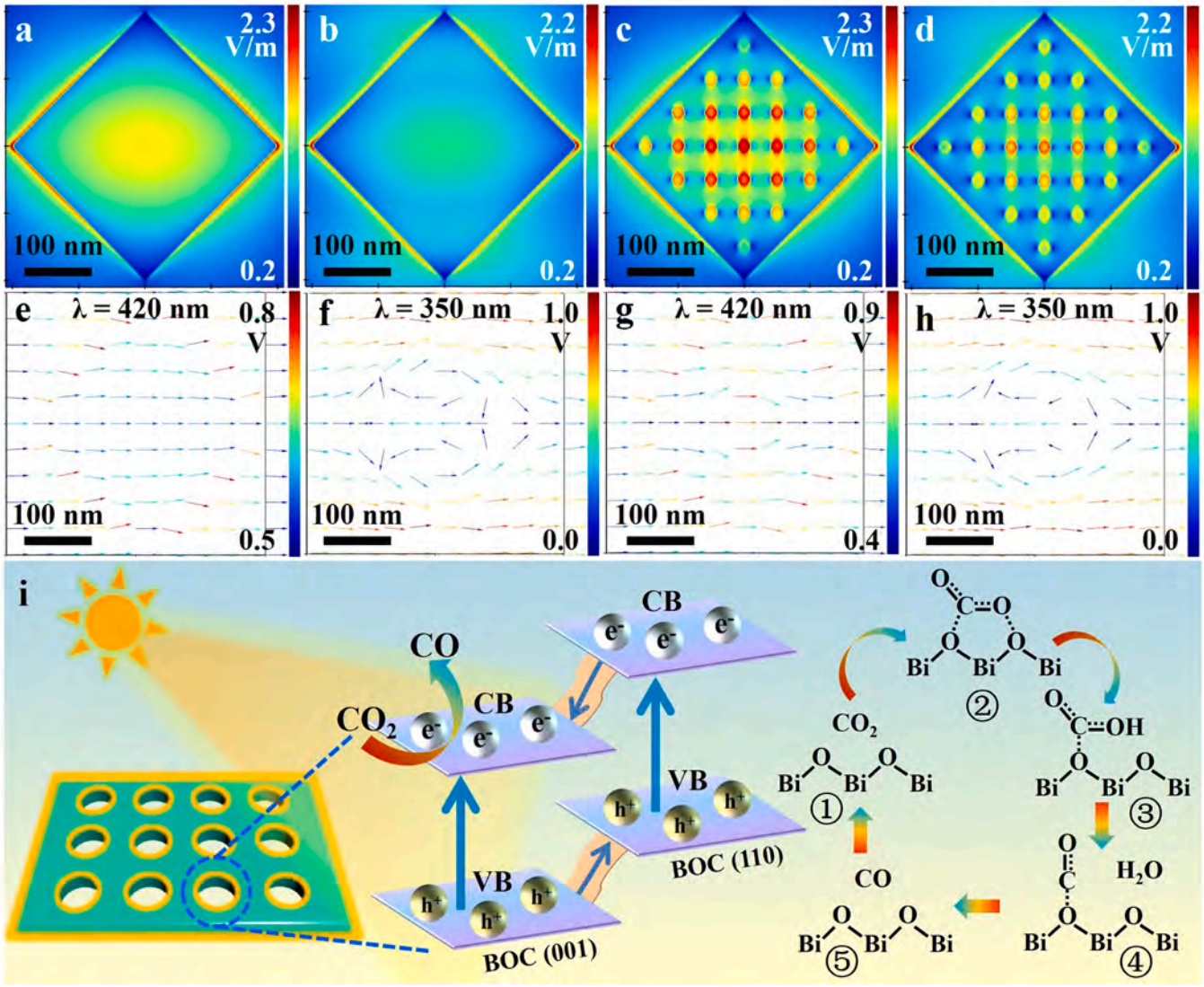

Fig. 5. Electric field distribution derived by FDTD simulation from (a, b) BOC-NS and (c, d) BOC-PNS at excitation wavelengths of (a, c) 420 and (b, d) 350 nm and electric-field vector at excitation wavelengths obtained by FDTD simulation for (e, f) BOC-NS and (g, h) BOC-PNS at excitation wavelengths of (e, g) 420 and (f, h) 350 nm, where E denotes the vector of the electric field. (i) Schematic illustration of the CO_2 conversion process on BOC-PNS.

Quan: Data curation, Investigation. **Gaopeng Liu:** Data curation, Investigation. **Xiaolin Zhang:** Data curation, Investigation. **Fangyu Xiong:** Investigation, Writing – original draft. **Chao Huang:** Investigation, Writing – original draft. **Mengxia Ji:** Resources, Supervision. **Huaming Li:** Resources, Supervision. **Paul K. Chu:** Resources, Writing – review & editing, Supervision. **Jiexiang Xia:** Conceptualization, Resources, Writing – review & editing, Supervision.

Declaration of Competing Interest

The authors declare that they have no known competing financial interests or personal relationships that could have appeared to influence the work reported in this paper.

Data Availability

Data will be made available on request.

Acknowledgments

This work was financially supported by the National Natural Science Foundation of China (No. 22108106, 22108108, 22108055, 21676128), Natural Science Foundation of Jiangsu Province (No. BK20220598, BK20210742), China Postdoctoral Science Foundation (No. 2020M680065), Hong Kong Scholar Program (No. XJ2021021), and City University of Hong Kong Donation Research Grant (DON-RMG No. 9229021).

Appendix A. Supporting information

Supplementary data associated with this article can be found in the online version at doi:10.1016/j.apcatb.2022.122304.

References

[1] M. Sayed, J.G. Yu, G. Liu, M. Jaroniec, Non-noble plasmonic metal-based photocatalysts, Chem. Rev. 122 (2022) 10484–10537, https://doi.org/10.1021/acs.chemrev.1c00473.
[2] E. Nikoloudakis, I. López-Duarte, G. Charalambidis, K. Ladomenou, M. Ince, A. G. Coutsolelos, Porphyrins and phthalocyanines as biomimetic tools for photocatalytic H_2 production and CO_2 reduction, Chem. Soc. Rev. 51 (2022) 6965–7045, https://doi.org/10.1039/D2CS00183G.
[3] C.Y. Feng, Z.P. Wu, K.W. Huang, J.H. Ye, H.B. Zhang, Surface modification of 2D photocatalysts for solar energy conversion, Adv. Mater. 34 (2022) 2200180, https://doi.org/10.1002/adma.202200180.

[4] H.J. Son, C. Pac, S.O. Kang, Inorganometallic photocatalyst for CO_2 reduction, Acc. Chem. Res. 54 (2021) 4530–4544, https://doi.org/10.1021/acs.accounts.1c00579.

[5] S.D. Sun, L.P. He, M. Yang, J. Cui, S.H. Liang, Facet junction engineering for photocatalysis: a comprehensive review on elementary knowledge, facet-synergistic mechanisms, functional modifications, and future perspectives, Adv. Funct. Mater. 32 (2022) 2106982, https://doi.org/10.1002/adfm.202106982.

[6] Z.S. Luo, X.Y. Ye, S.J. Zhang, S.K. Xue, C. Yang, Y.D. Hou, W.D. Xing, R. Yu, J. Sun, Z.Y. Yu, X.C. Wang, Unveiling the charge transfer dynamics steered by built-in electric fields in BiOBr photocatalysts, Nat. Commun. 13 (2022) 2230, https://doi.org/10.1038/s41467-022-29825-0.

[7] M. Li, S.X. Yu, H.W. Huang, X.W. Li, Y.B. Feng, C. Wang, Y.G. Wang, T.Y. Ma, L. Guo, Y.H. Zhang, Unprecedented eighteen-faceted BiOCl with a ternary facet junction boosting cascade charge flow and photo-redox, Angew. Chem. Int. Ed. 58 (2019) 9517–9521, https://doi.org/10.1002/anie.201904921.

[8] Z.J. Xie, B. Zhang, Y.Q. Ge, Y. Zhu, G.H. Nie, Y.F. Song, C.K. Lim, H. Zhang, P. N. Prasad, Chemistry, functionalization, and applications of recent monoelemental two-dimensional materials and their heterostructures, Chem. Rev. 122 (2022) 1127–1207, https://doi.org/10.1021/acs.chemrev.1c00165.

[9] W.C. Wang, Y. Tao, J.C. Fan, Z.P. Yan, H. Shang, D.L. Phillips, M. Chen, G.S. Li, Fullerene–graphene acceptor drives ultrafast carrier dynamics for sustainable CdS photocatalytic hydrogen evolution, Adv. Funct. Mater. 32 (2022) 2201357, https://doi.org/10.1002/adfm.202201357.

[10] C. Xiao, B.A. Lu, P. Xue, N. Tian, Z.Y. Zhou, X. Lin, W.F. Lin, S.G. Sun, High-index-facet- and high-surface-energy nanocrystals of metals and metal oxides as highly efficient catalysts, Joule 4 (2020) 2562–2598, https://doi.org/10.1016/j.joule.2020.10.002.

[11] C. Fu, F. Li, J.C. Zhang, D. Li, K. Qian, Y. Liu, J.W. Tang, F.T. Fan, Q. Zhang, X. Q. Gong, W.X. Huang, Site sensitivity of interfacial charge transfer and photocatalytic efficiency in photocatalysis: methanol oxidation on anatase TiO_2 nanocrystals, Angew. Chem. Int. Ed. 60 (2021) 6160–6169, https://doi.org/10.1002/anie.202014037.

[12] J.Z. Meng, Y.Y. Duan, S.J. Jing, J.P. Ma, K.W. Wang, K. Zhou, C.G. Ban, Y. Wang, B. H. Hu, D.M. Yu, L.Y. Gan, X.Y. Zhou, Facet junction of BiOBr nanosheets boosting spatial charge separation for CO_2 photoreduction, Nano Energy 92 (2022), 106671, https://doi.org/10.1016/j.nanoen.2021.106671.

[13] M.S. Lodge, S.A. Yang, S. Mukherjee, B. Weber, Atomically thin quantum spin hall insulators, Adv. Mater. 33 (2021) 2008029, https://doi.org/10.1002/adma.202008029.

[14] M. Zhang, G.M. Biesold, Z.Q. Lin, A multifunctional 2D black phosphorene-based platform for improved photovoltaics, Chem. Soc. Rev. 50 (2021) 13346–13370, https://doi.org/10.1039/D1CS00847A.

[15] A. Fali, T.Y. Zhang, J.P. Terry, E. Kahn, K. Fujisawa, B. Kabius, S. Koirala, Y. Ghafouri, D. Zhou, W.S. Song, L. Yang, M. Terrones, Y. Abate, Photodegradation protection in 2D in-plane heterostructures revealed by hyperspectral nanoimaging: the role of nanointerface 2D alloys, ACS Nano 15 (2021) 2447–2457, https://doi.org/10.1021/acsnano.0c06148.

[16] J. Jiang, K. Zhao, X.Y. Xiao, L.Z. Zhang, Synthesis and facet-dependent photoreactivity of BiOCl single-crystalline nanosheets, J. Am. Chem. Soc. 134 (2012) 4473–4476, https://doi.org/10.1021/ja210484t.

[17] H. Li, J. Li, Z.H. Ai, F.L. Jia, L.Z. Zhang, Oxygen vacancy-mediated photocatalysis of BiOCl: reactivity, selectivity, and perspectives, Angew. Chem. Int. Ed. 57 (2018) 122–138, https://doi.org/10.1002/anie.201705628.

[18] N. Tian, C. Hu, J.J. Wang, Y.H. Zhang, T.Y. Ma, H.W. Huang, Layered bismuth-based photocatalysts, Coord. Chem. Rev. 463 (2022), 214515, https://doi.org/10.1016/j.ccr.2022.214515.

[19] S. Vinoth, W.J. Ong, A. Pandikumar, Defect engineering of BiOX (X = Cl, Br, I) based photocatalysts for energy and environmental applications: Current progress and future perspectives, Coord. Chem. Rev. 464 (2022), 214541, https://doi.org/10.1016/j.ccr.2022.214541.

[20] J.P. Perdew, K. Burke, M. Ernzerhof, Generalized gradient approximation made simple, Phys. Rev. Lett. 77 (1996) 3865–3868, https://doi.org/10.1103/PhysRevLett.77.3865.

[21] G. Kresse, D. Joubert, From ultrasoft pseudopotentials to the projector augmented-wave method, Phys. Rev. B 59 (1999) 1758–1775, https://doi.org/10.1103/PhysRevB.59.1758.

[22] P.E. Blöchl, Projector augmented-wave method, Phys. Rev. B 50 (1994) 17953–17979, https://doi.org/10.1103/PhysRevB.50.17953.

[23] X.G. Liu, Y.J. Li, L. Zeng, X. Li, N. Chen, S.B. Bai, H.N. He, Q. Wang, C.H. Zhang, A review on mechanochemistry: approaching advanced energy materials with greener force, Adv. Mater. (2022) 2108327, https://doi.org/10.1002/adma.202108327.

[24] H. Li, J. Shang, H.J. Zhu, Z.P. Yang, Z.H. Ai, L.Z. Zhang, Oxygen vacancy structure associated photocatalytic water oxidation of BiOCl, ACS Catal. 6 (2016) 8276–8285, https://doi.org/10.1021/acscatal.6b02613.

[25] Y. j Zhang, Z.F. Xu, Q. Wang, W.C. Hao, X.P. Zhai, X. Fei, X.J. Huang, Y.P. Bi, Unveiling the activity origin of ultrathin BiOCl nanosheets for photocatalytic CO_2 reduction, Appl. Catal. B: Environ. 299 (2021), 120679, https://doi.org/10.1016/j.apcatb.2021.120679.

[26] L. Zhang, W.Z. Wang, D. Jiang, E.P. Gao, S.M. Sun, Photoreduction of CO_2 on BiOCl nanoplates with the assistance of photoinduced oxygen vacancies, Nano Res 8 (2015) 821–831, https://doi.org/10.1007/s12274-014-0564-2.

[27] B. Wang, S.Z. Yang, H.L. Chen, Q. Gao, Y.X. Weng, W.S. Zhu, G.P. Liu, Y. Zhang, Y. Z. Ye, H.Y. Zhu, H.M. Li, J.X. Xia, Revealing the role of oxygen vacancies in bimetallic $PbBiO_2Br$ atomic layers for boosting photocatalytic CO_2 conversion, Appl. Catal. B: Environ. 277 (2020), 119170, https://doi.org/10.1016/j.apcatb.2020.119170.

[28] G.C. Jiang, J. Wang, N.Y. Li, R. Hübner, M. Georgi, B. Cai, Z.Q. Li, V. Lesnyak, N. Gaponik, A. Eychmüller, Self-supported three-dimensional quantum dot aerogels as a promising photocatalyst for CO_2 reduction, Chem. Mater. 34 (2022) 2687–2695, https://doi.org/10.1021/acs.chemmater.1c04028.

[29] B. Wang, W. Zhang, G.P. Liu, H.L. Chen, Y.X. Weng, H.M. Li, P.K. Chu, J.X. Xia, Excited electron-rich $Bi^{(3-x)+}$ sites: a quantum well-like structure for highly-promoted selective photocatalytic CO_2 reduction performance, 202202885, Adv. Funct. Mater. 32 (2022), https://doi.org/10.1002/adfm.202202885.

[30] J. Di, C. Chen, S.Z. Yang, M.X. Ji, C. Yan, K.Z. Gu, J.X. Xia, H.M. Li, S.Z. Li, Z. Liu, Defect engineering in atomically-thin bismuth oxychloride towards photocatalytic oxygen evolution, J. Mater. Chem. A 5 (2017) 14144–14151, https://doi.org/10.1039/c7ta03624h.

[31] B. Wang, J.Z. Zhao, H.L. Chen, Y.X. Weng, H. Tang, Z.R. Chen, W.S. Zhu, J.X. Xia, H.M. Li, Unique Z-scheme carbonized polymer dots/$Bi_4O_5Br_2$ hybrids for efficiently boosting photocatalytic CO_2 reduction, Appl. Catal. B Environ. 293 (2021), 120182, https://doi.org/10.1016/j.apcatb.2021.120182.

[32] D. Li, X.F. Chen, Y.Z. Lv, G.Y. Zhang, Y. Huang, W. Liu, Y. Li, R.S. Chen, C. Nuckolls, H.W. Ni, An effective hybrid electrocatalyst for the alkaline HER: highly dispersed Pt sites immobilized by a functionalized NiRu-hydroxide, Appl. Catal. B: Environ. 269 (2020), 118824, https://doi.org/10.1016/j.apcatb.2020.118824.

[33] G.P. Liu, B. Wang, X.W. Zhu, P.H. Ding, J.Z. Zhao, H.M. Li, Z.R. Chen, W.S. Zhu, J. X. Xia, Edge-site-rich ordered macroporous BiOCl triggers C$\overline{\text{—}}$O activation for efficient CO_2 photoreduction, Small 18 (2022) 2105228, https://doi.org/10.1002/smll.202105228.

[34] J.T. Dong, F. Chen, L. Xu, P.C. Yan, J.C. Qian, Y. Chen, M.Y. Yang, H.N. Li, Fabrication of sensitive photoelectrochemical aptasensor using Ag nanoparticles sensitized bismuth oxyiodide for determination of chloramphenicol, Microchem. J. 178 (2022) 107317, https://doi.org/10.1016/j.microc.2022.107317.

[35] Y.N. Liu, Q. Li, Z.C. Lian, J.C. Fan, Y. Tao, G.S. Li, H.X. Li, Polarization field promoted photoelectrocatalysis for synergistic environmental remediation and H_2 production, Chem. Eng. J. 437 (2022), 135132, https://doi.org/10.1016/j.cej.2022.135132.

[36] X.W. Zhu, J.M. Yang, X.L. Zhu, J.J. Yuan, M. Zhou, X.J. She, Q. Yu, Y.H. Song, Y. B. She, Y.J. Hua, H.M. Li, H. Xu, Exploring deep effects of atomic vacancies on activating CO_2 photoreduction via rationally designing indium oxide photocatalysts, Chem. Eng. J. 422 (2021), 129888, https://doi.org/10.1016/j.cej.2021.129888.

[37] Y. Zhang, J.Di, X. W. Zhu, M. X. Ji, C. Chen, Y. N. Liu, L. N. Li, T. G. Wei, H. M. Li, J. X. Xi, Chemical bonding interface in $Bi_2Sn_2O_7$/BiOBr S-scheme heterojunction triggering efficient N_2 photofixation, Appl. Catal. B Environ. 323 (2023) 122148, doi: 10.1016/j.apcatb.2022.122148.

[38] J.C. Zhu, W.W. Shao, X.D. Li, X.C. Jiao, J.F. Zhu, Y.F. Sun, Y. Xie, Asymmetric triple-atom sites confined in ternary oxide enabling selective CO_2 photothermal reduction to acetate, J. Am. Chem. Soc. 143 (2021) 18233–18241, https://doi.org/10.1021/jacs.1c08033.

[39] P.F. Xia, B.C. Zhu, J.G. Yu, S.W. Cao, M. Jaroniec, Ultra-thin nanosheet assemblies of graphitic carbon nitride for enhanced photocatalytic CO_2, Reduct., J. Mater. Chem. A 5 (2017) 3230, https://doi.org/10.1039/c6ta08310b.

[40] J. Wu, X.D. Li, W. Shi, P.Q. Ling, Y.F. Sun, X.C. Jiao, S. Gao, L. Liang, J.Q. Xu, W. S. Yan, C.M. Wang, Y. Xie, Efficient visible-light-driven CO_2 reduction mediated by defect-engineered BiOBr atomic layers, Angew. Chem., Int. Ed. 57 (2018) 8719, https://doi.org/10.1002/anie.201803514.

[41] M.P. Jiang, K.K. Huang, J.H. Liu, D. Wang, Y. Wang, X. Wang, Z.D. Li, X.Y. Wang, Z.B. Geng, X.Y. Hou, S.H. Feng, Magnetic-field-regulated TiO_2 {100} facets: a strategy for C-C coupling in CO_2 photocatalytic conversion, Chem 6 (2020) 2335–2346, https://doi.org/10.1016/j.chempr.2020.06.033.

[42] Z.Y. Ma, P.H. Li, L.Q. Ye, Y. Zhou, F.Y. Su, C.H. Ding, H.Q. Xie, Y. Bai, P.K. Wong, Oxygen vacancies induced exciton dissociation of flexible BiOCl nanosheets for effective photocatalytic CO_2 conversion, J. Mater. Chem. A 5 (2017) 24995–25004, https://doi.org/10.1039/C7TA08766G.

[43] P.O. Graf, D.J.M. de Vlieger, B.L. Mojet, L. Lefferts, New insights in reactivity of hydroxyl groups in water gas shift reaction on Pt/ZrO_2, J. Catal. 262 (2009) 181–187, https://doi.org/10.1016/j.jcat.2008.12.015.

[44] M. El-Maazawi, A.N. Finken, A.B. Nair, V.H. Grassian, Adsorption and photocatalytic oxidation of acetone on TiO_2: an in situ transmission FT-IR study, J. Catal. 191 (2000) 138–146, https://doi.org/10.1006/jcat.1999.2794.

[45] B. Bachiller-Baeza, I. Rodriguez-Ramos, A. Guerrero-Ruiz, Interaction of carbon dioxide with the surface of zirconia polymorphs, Langmuir 14 (1998) 3556–3564, https://doi.org/10.1021/la970856q.

[46] A.A. Tsyganenko, V.N. Filimonov, Infrared spectra of surface hydroxyl groups and crystalline structure of oxides, Spectrosc. Lett. 5 (1972) 477–487, https://doi.org/10.1080/00387017208065418.

[47] C.Y. Xu, W.H. Huang, Z. Li, B.W. Deng, Y.W. Zhang, M.J. Ni, K.F. Cen, Photothermal coupling factor achieving CO_2 reduction based on palladium-nanoparticle-loaded TiO_2, ACS Catal. 8 (2018) 6582–6593, https://doi.org/10.1021/acscatal.8b00272.

[48] Q. Yu, T.Y. Peng, J.F. Zhang, X.X. Liu, Y. Pan, D.F. Ge, L. Zhao, F. Rosei, J. M. Zhang, $Cu_{2-x}S_x$ capped AuCu nanostars for efficient plasmonic photothermal tumor treatment in the second near-infrared window, Small 18 (2022) 2103174, https://doi.org/10.1002/smll.202103174.

Supporting Information

Porous edge confinement: High carrier potential and low activation energy barrier synergistically boosting the efficiency of selective photocatalytic CO_2 conversion

Bin Wang[a,b,1], Xingwang Zhu[c,1], Fangcheng Huang[d], Yu Quan[a], Gaopeng Liu[a], Xiaolin Zhang[b], Fangyu Xiong[b], Chao Huang[b], Mengxia Ji[a], Huaming Li[a], Paul K. Chu[b,*], Jiexiang Xia[a,*]

[a] *School of Chemistry and Chemical Engineering, Institute for Energy Research, Jiangsu University, 301 Xuefu Road, Zhenjiang 212013, China*

[b] *Department of Physics, Department of Materials Science and Engineering, and Department of Biomedical Engineering, City University of Hong Kong, Tat Chee Avenue, Kowloon, Hong Kong, China*

[c] *College of Environmental Science and Engineering, Yangzhou University, Yangzhou 225009, P. R. China*

[d] *Department of Information Engineering, Electronics and Telecommunications, Sapienza University of Rome, Piazzale Aldo Moro 5, 00185 Roma, Italy*

[1] These authors contributed equally to this work.

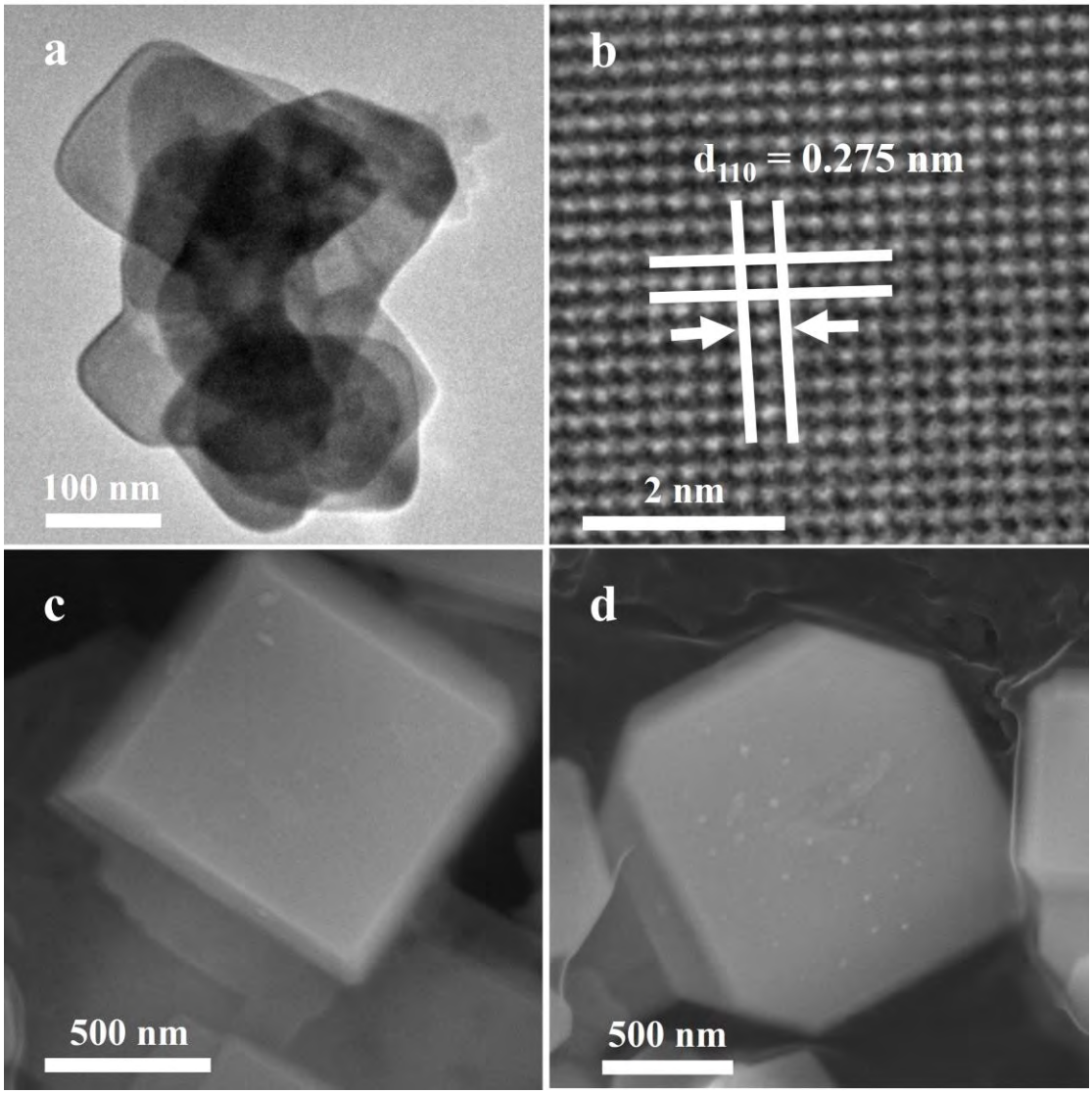

Fig. S1 (a) TEM and (b) HR-TEM images of BOC-NS; (c, d) SEM images of BOC-NP.

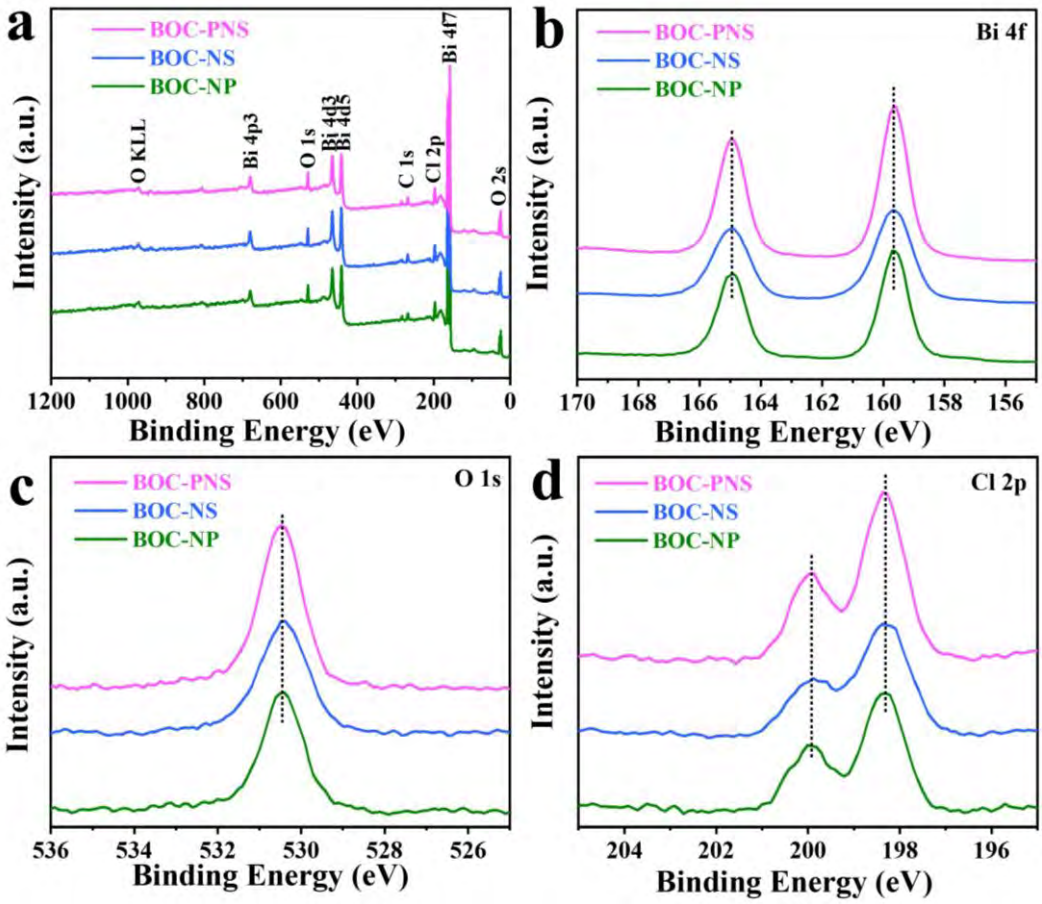

Fig. S2. XPS spectra of BOC-NP, BOC-NS, and BOC-PNS: (a) Survey, (b) Bi 4*f*, (c) O 1*s*, and (d) Cl 2*p*.

XPS is conducted to analyze the surface chemical composition and chemical states of the materials. As shown in **Fig. S2a**, the BOC materials are composed of three major elements: Bi, O, and Cl. The high-resolution Bi 4*f* spectra show peaks of Bi $4f_{7/2}$ and Bi $4f_{5/2}$ at 159.5 and 164.9 eV, respectively (**Fig. S2b**) corresponding to Bi^{3+} [S1]. The O 1*s* peak at 530.5 eV is related to Bi-O (**Fig. S2c**) [S2] and the C1 $2p_{3/2}$ and C1 $2p_{1/2}$ peaks at 198.3 eV and 199.7 eV are associated with Cl^- (**Fig. S2d**) Cl^- [S3].

[S1] S. W. Cao, B. J. Shen, T. Tong, J. W. Fu, J. G. Yu 2D/2D Heterojunction of Ultrathin MXene/Bi_2WO_6 Nanosheets for Improved Photocatalytic CO_2 Reduction, Adv. Funct. Mater. 28 (2018) 1800136.

[S2] L. Hao, L. Kang, H. W. Huang, L. Q. Ye, K. L. Han, S. Q. Yang, H. J. Yu, M. Batmunkh, Y. H. Zhang, T. Y. Ma, Surface-Halogenation-Induced Atomic-Site Activation and Local Charge Separation for Superb CO_2 Photoreduction, Adv. Mater. 31 (2019) 1900546.

[S3] Xu Z K, Lin S Y, Construction of AgCl/Ag/BiOCl with a concave-rhombicuboctahedron core-shell hierarchitecture and enhanced photocatalytic activity, RSC Adv. 7 (2017) 9512-9512.

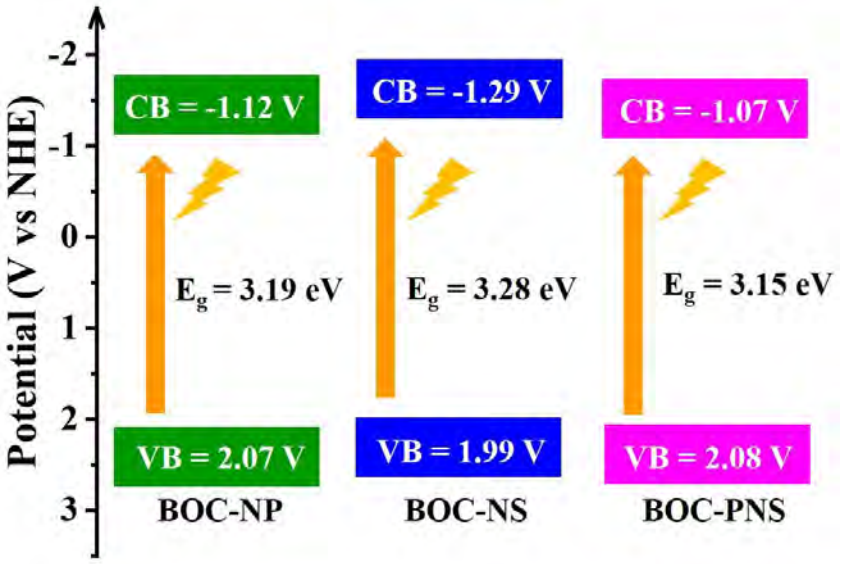

Fig. S3. Schematic diagram of the band structure of BOC-NP, BOC-NS, and BOC-PNS.

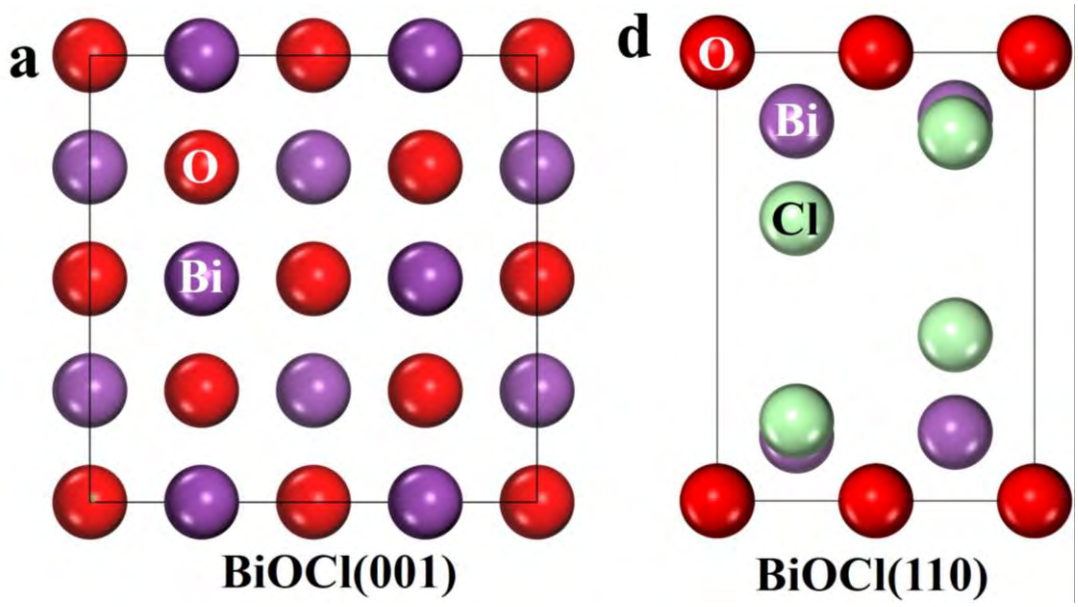

Fig. S4. Top view schematics of (a) BiOCl (001) and (b) BiOCl (110).

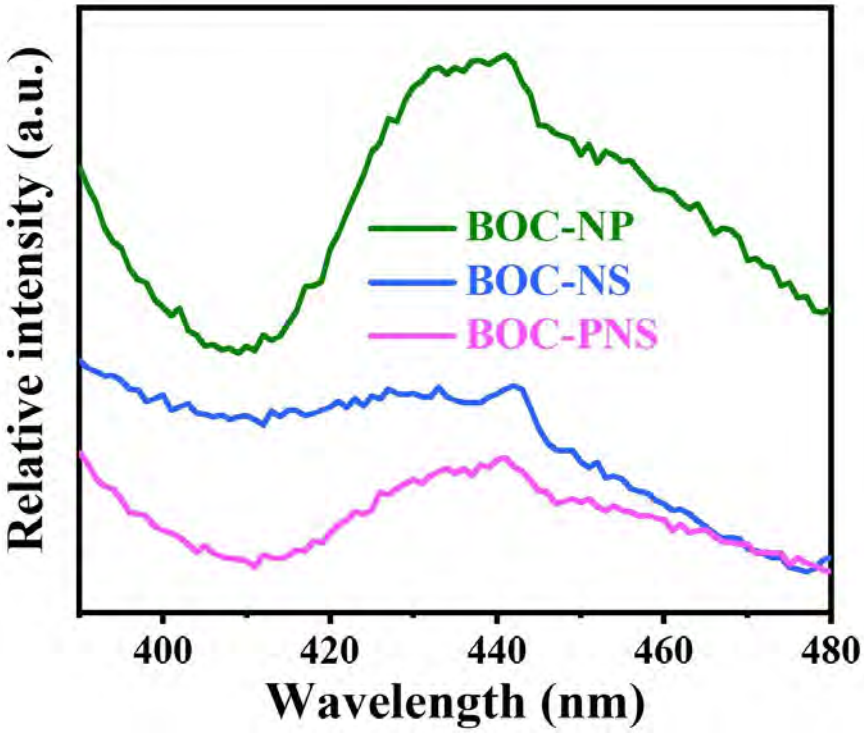

Fig. S5. PL spectra of BOC-PNS, BOC-NS, and BOC-NP.

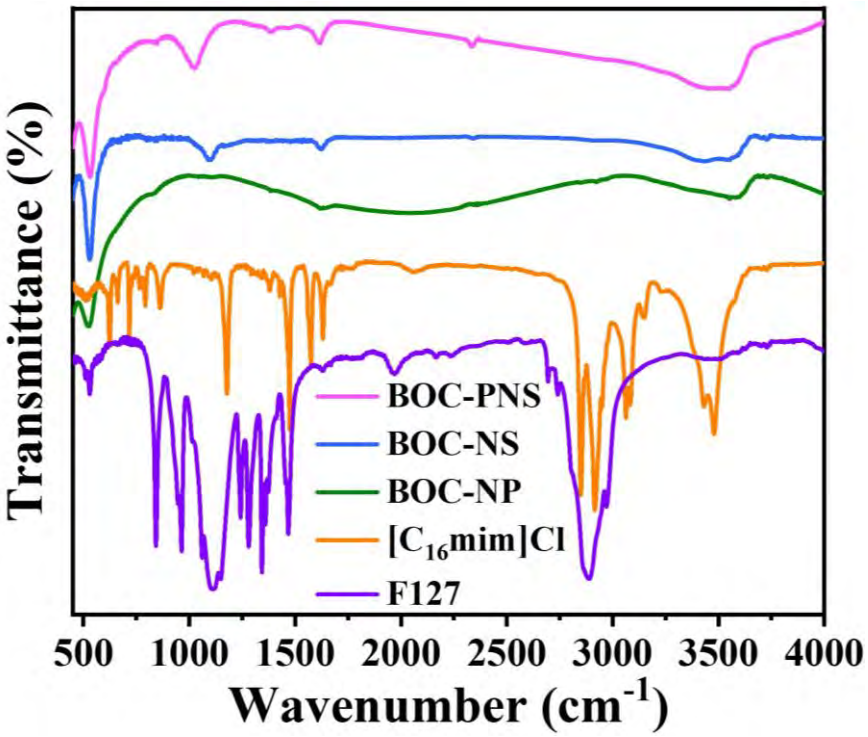

Fig. S6. FTIR spectra of BOC-PNS, BOC-NS, BOC-NP, [C_{16}mim]Cl, and F127.

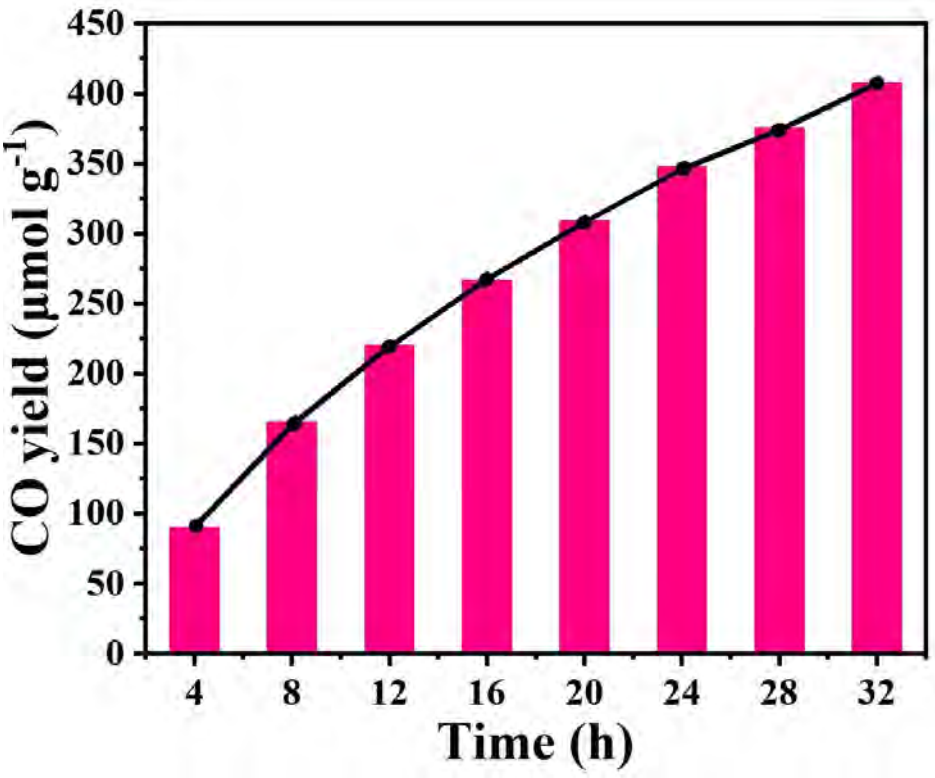

Fig. S7. Stability of CO_2 photoreduction in the presence of BOC-PNS.

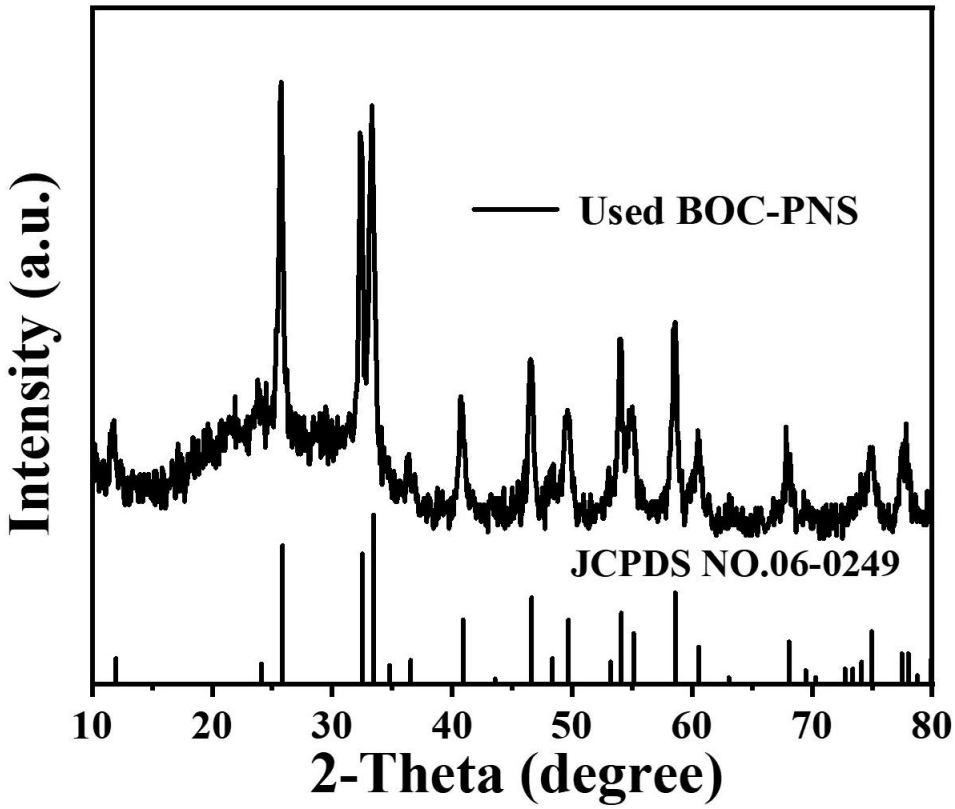

Fig. S8. XRD patterns of BOC-PNS after the photocatalytic CO_2 reduction stability test.

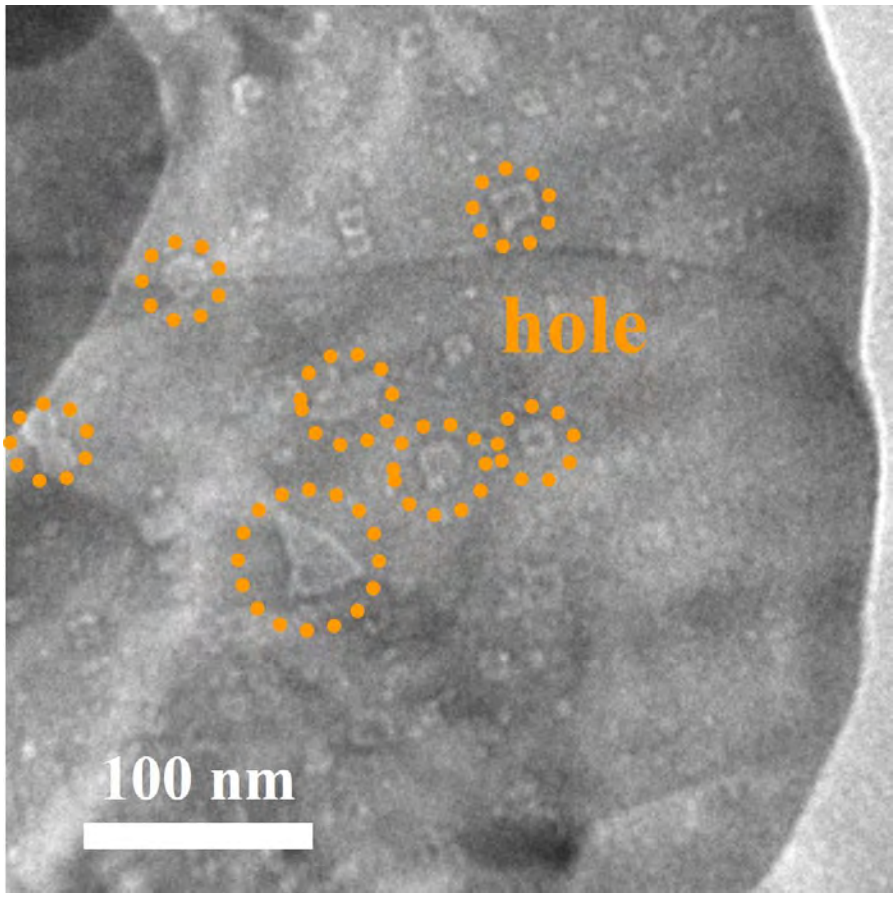

Fig. S9. TEM image of BOC-PNS after the photocatalytic CO_2 reduction stability test.

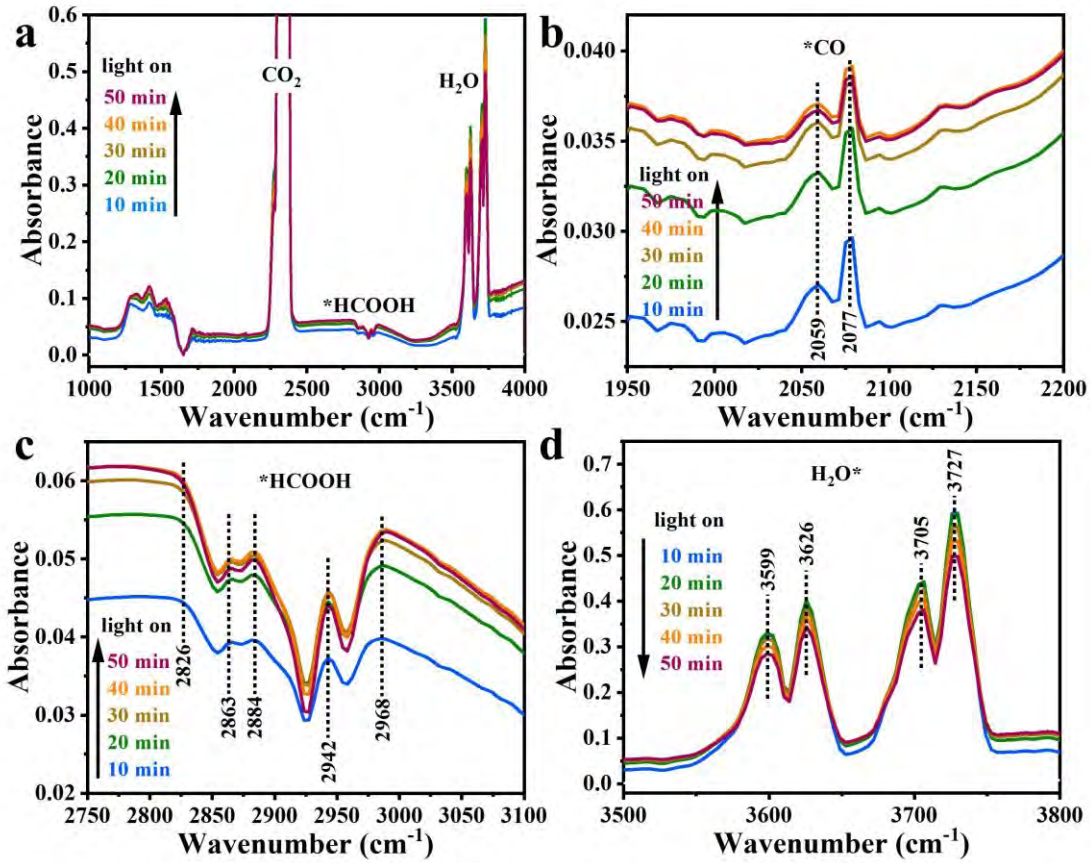

Fig. S10 *In situ* FTIR spectra in different wavenumber ranges acquired from BOC-PNS for simulated solar-driven CO_2 reduction.

Table S1. Comparison of the reaction conditions and characteristics with other photocatalysts for photocatalytic CO_2 conversion.

Photocatalysts	Dosages	Light sources	Products	Yields ($\mu mol\ g^{-1}\ h^{-1}$)	Refs.
BOC-PNS **BOC-NS** **BOC-NP**	30 mg	300 W Xe lamp	CO	28.2 13.5 9.9	**Our work**
ROV DUC PBOC-1	20 mg	300 W Xe lamp	CO	16.02	*Adv. Funct. Mater.* **2022**, 2202885
BiOCl	100 mg	500 W Xe lamp	CO CH_4	1.00 0.15	*Nano Res.* **2015**, 8, 821-831
BiOBr	150 mg	300 W Xe lamp $\lambda > 400$ nm	CO CH_4	1.68 0.17	*Appl. Catal. B Environ.* **2016**, 187, 281-290
$Bi_4O_5Br_2$	150 mg	300 W Xe lamp $\lambda > 400$ nm	CO CH_4	2.73 2.04	*Appl. Catal. B Environ.* **2016**, 187, 281-290
BiOI	100 mg	300 W Xe lamp	CH_4	1.98	*Mater. Res. Bull.* **2014**, 55, 43-47.
few-layered BiOI	150 mg	300 W Xe lamp $\lambda > 420$ nm	CO CH_4	4.1 0.42	*Sol. Energy Mater Sol. Cells* **2016**, 144, 732-739
7.4-BiOI/g-C_3N_4	100 mg	300 W Xe lamp $\lambda > 400$ nm	CO	3.58	*ACS Appl. Mater. Interfaces* **2016**, 8, 3765-3775
BiOI-001	50 mg	300 W Xe lamp	CO CH_4	5.18 1.78	*Chem. Eng. J.* **2016**, 291, 39-46
Oxygen-deficient BiOBr	-	500 W Xe lamp $\lambda > 400$ nm	CH_4	0.486	*ChemCatChem* **2016**, 8, 3074-3081
g-C_3N_4/BiOBr/Au-S	100 mg	300 W Xe lamp $\lambda > 380$ nm	CO CH_4	2.63 0.52	*Sol. Energy Mater Sol. Cells* **2016**, 157, 406-414
BiOBr-4-001	50 mg	300 W Xe lamp	CO	4.45	*Catal. Sci. Technol.* **2017**, 7, 265-271
Ultrathin BiOCl	50 mg	300 W Xe lamp	CO CH_4	14.25 1.125	*J. Taiwan Inst. Chem. E.* **2017**, 78, 395-400
BiOCl-OV	50 mg	300 W Xe lamp	CO	8.76	*J. Mater. Chem. A* **2017**, 5, 24995-25004
AuNR/001T/BV-NF	200 mg	300 W Xe lamp	CO CH_4	2.5 7.5	*J. Mater. Chem. A* **2018**, 6, 11838-11845
oxygen-deficient BiOBr atomic layers	100 mg	300 W Xe lamp $\lambda > 400$ nm	CO	87.4	*Angew. Chem. Int. Ed.* **2018**, 57, 8719-8723
$BiOBr_{0.6}Cl_{0.4}$ **BiOCl**	10 mg	300 W Xe lamp	CO	15.86 2.11	*Appl. Catal. B Environ.* **2019**, 243, 734-740

BiOBr				1.55	
BiOCl-Ag-E **BiOCl-Ag-S** **BiOCl**	50 mg	300 W Xe lamp	CO	20 12 7	*Nano Energy* **2019**, 57, 398-404
Bi_2WO_6-OV/BiOI **Bi_2WO_6-OV** **BiOI**	-	500 W Xe lamp λ > 400 nm	CH_4	2.29 1.02 0.32	*Chem. Eng. J.* **2019**, 372, 1183-1193
P/Bi-BiOBr-0.25	50 mg	500 W Xe lamp λ > 300 nm	CO CH_4	3.14 0.49	*ACS Sustainable Chem. Eng.* **2019**, 7, 14953-14961
V_{Bi}-BiOBr UNs **BiOBr UNs**	30 mg	300 W Xe lamp	CO	20.1 5.3	*ACS Appl. Mater. Interfaces* **2019**, 11, 30786-30792
CN-BiOBr-OV	10 mg	300 W Xe lamp	CO CH_4	61.8 27.1	*Angew. Chem. Int. Ed.* **2020**, 59, 4519-4524
CN/BOC-OV	20 mg	300 W Xe lamp	CO CH_4	4.73 0.77	*ACS Appl. Energy Mater.* **2020**, 3, 4610-4618
BiOBr	10 mg	300 W Xe lamp	CO CH_4	21.6 1.2	*Appl. Catal. B Environ.* **2020**, 274, 119063
BiOBr-NS	-	300 W Xe lamp λ > 400 nm	CH_4	0.39	*ACS Appl. Mater. Interfaces* **2020**, 12, 26991-27000
BiOBr **BiOBr/Gd-0.05**	100 mg	300 W Xe lamp λ > 420 nm	CH_3OH	8.03 41.24	*Chem. Eng. J.* **2020**, 400, 125944
BiOBr **Co_2N/BiOBr-1**	30 mg	300 W Xe lamp	CO	11.2 67.8	*Nano Energy* **2021**, 79, 105429
BiOBr **OV-BiOBr-3**	30 mg	300 W Xe lamp λ > 400 nm	CO	1.02 2.03	*Sol. RRL* **2021**, 5, 2000480
BiOCl@Bi_2O_3 **BiOCl**	50 mg	300 W Xe lamp	CO	75 52	*Adv. Mater.* **2020**, 32, 2004311
0.25% Au/BiOCl-OV	50 mg	300 W Xe lamp	CO CH_4	3.46 1.39	*Nanoscale* **2021**, 13, 2585-2592
120BiOBr	10 mg	300 W Xe lamp	CO CH_4	88.1 5.8	*J. Colloid. Interf. Sci.* **2021**, 593, 231-243
BiOBr/La-4.9%	100 mg	300 W Xe lamp λ > 420 nm	CH_3OH	63.12	*Chem. Eng. J.* **2021**, 418, 129286
10% pCN/BiOBr	20 mg	300 W Xe lamp	CH_3OH	267.02	*Appl. Surf. Sci.* **2021**, 556, 149828
50%-BiOBr-VO/HNb_3O_8	50 mg	300 W Xe lamp	CO	32.92	*J. Colloid. Interf. Sci.* **2021**, 599, 245-254
C_3N_4/bismuthene/BiOCl	2 mg	300 W Xe lamp	CO CH_4	71 61	*ACS Appl. Mater. Interfaces* **2021**, 13, 21582-21592
BOC-250	30 mg	300 W Xe lamp	CO	24.82	*Appl. Catal. B Environ.* **2021**, 297, 120413
a-BiOCl	50 mg	300 W Xe lamp	CO	8.99	*Appl. Catal. B Environ.* **2021**, 297, 120426
BiOCl-B-OV	50 mg	300 W Xe lamp	CO	83.64	*Adv. Mater.* **2021**, 33, 2100143

		λ > 400 nm			
BiOBr/NiO	20 mg	300 W Xe lamp	CO CH_4	6.6 12.8	*Sol. RRL* **2022**, 6, 2100587
PVP-BiOBr	10 mg	300 W Xe lamp	CO CH_4	263.2 3.3	*J. Colloid. Interf. Sci.* **2022**, 606, 1087-1100
Ultrathin BiOCl nanosheets	10 mg	300 W Xe lamp	CO CH_4	21.36 Trace	*Appl. Catal. B Environ.* **2021**, 299, 120679
BiOCl-0.6	10 mg	300 W Xe lamp λ > 400 nm	CO	14.88	*J. Taiwan Inst. Chem. E.* **2021**, 128, 380-387
AgBr/BiOBr	10 mg	300 W Xe lamp	CO CH_4	212.6 5.7	*Appl. Catal. B Environ.* **2022**, 301, 120802
VDWGs-rich BiOCl atomic layers	50 mg	300 W Xe lamp λ > 400 nm	CO	188.2	*Nat. Commun.* **2021**, 12, 5923
BiOBr-5	10 mg	300 W Xe lamp	CO	3.25	*Nano Energy* **2022**, 92, 106671
BiOCl-P	30 mg	300 W Xe lamp	CO CH_4	19.52 0.76	*Small* **2022**, 18, 2105228
CuO/BiOCl	50 mg	300 W Xe lamp	CH_4 CH_3OH	114.1 36.2	*Appl. Surf. Sci.* **2022**, 583, 152463
Bi vacancies BiOCl	20 mg	300 W Xe lamp	CO	21.99	*Nano Lett.* **2021**, 21, 10260-10266
$CsPbBr_3$/BiOBr	8 mg	300 W Xe lamp λ > 420 nm	CO CH_4	26.1 2.5	*Inorg. Chem.* **2022**, 61, 3351-3360
CdS/BiOCl	50 mg	300 W Xe lamp	CO CH_4	2.00 6.85	*ACS Appl. Energy Mater.* **2022**, 5, 1149-1158
g-C_3N_4/20-$Bi_4O_5I_2$	100 mg	300 W Xe lamp	CO	45.6	*Appl. Catal. B Environ.* **2016**, 194, 98-104
Hollow $Bi_4O_5Br_2$	50 mg	300 W Xe lamp	CO CH_4	3.16 0.5	*Nano Energy* **2019**, 64, 103955
$Bi_4O_5Br_2$/Fe-MIL-5	20 mg	300 W Xe lamp	CO CH_4	0.023 7.96	*Catal. Sci. Technol.* **2021**, 11, 2864-2872
8 wt% CPDs/$Bi_4O_5Br_2$	30 mg	300 W Xe lamp	CO	132.42	*Appl. Catal. B Environ.* **2021**, 293, 120182
$Bi_4O_5Br_2$-UN	20 mg	300 W Xe lamp	CO CH_4	31.565 Trace	*Chem. Eng. J.* **2019**, 360, 473-482
$Bi_4O_5I_2$	100 mg	300 W Xe lamp λ > 400 nm	CO CH_4	19.82 0.22	J. CO_2 Util. **2016**, 14, 135-142
Bi_5O_7I	100 mg	300 W Xe lamp λ > 400 nm	CO CH_4	1.73 0.18	J. CO_2 Util. **2016**, 14, 135-142
BiOI	100 mg	300 W Xe lamp λ > 400 nm	CO CH_4	0.70 0.27	J. CO_2 Util. **2016**, 14, 135-142
$Bi_4O_5I_2$−Fe30	50 mg	300 W Xe lamp	CO CH_4	23.77 4.98	*ACS Materials Lett.* **2021**, 3, 364-371
$Bi_4O_5I_2$	50 mg	300 W Xe	CO	4.21	*ACS Materials Lett.* **2021**, 3,

		lamp	CH_4	Trace	364-371
$Bi_4O_5I_2$-1.95	50 mg	300 W Xe lamp	CO CH_4	40.02 7.19	J. CO_2 Util. **2018**, 23, 51-60
$Bi_{24}O_{31}Cl_{10}$-OV	50 mg	300 W Xe lamp	CO	0.9	*ChemSusChem* **2019**, 12, 2740-2747
Bi_3O_4Cl/20%g-C_3N_4	50 mg	300 W Xe lamp	CO CH_4	6.6 1.9	*Chem. Eng. J.* **2021**, 409, 128178
CPDs/$Bi_{12}O_{17}Cl_2$	30 mg	300 W Xe lamp $\lambda > 400$ nm	CO	3.2	*CHEM. ENG. SCI.* **2021**, 232, 116338
PGCN/BOC 450	50 mg	300 W Xe lamp $\lambda > 420$ nm	CH_4	24.4	*J. Colloid. Interf. Sci.* **2021**, 585, 684-693
$Bi_{12}O_{17}Cl_2$ nanotubes	30 mg	300 W Xe lamp	CO	48.6	*Angew. Chem. Int. Ed.* **2018**, 57, 14847-14851
V_{BiO}-$Bi_{24}O_{31}Br_{10}$	30 mg	300 W Xe lamp	CO	24.9	*Adv. Energy Mater.* **2021**, 11, 2102389
CoPc@$Bi_{24}O_{31}Br_{10}$	100 mg	20 W LED white light	CH_3OH	145.2	*Dalton Trans.* **2019**, 48, 4941-4948
Co–Bi_3O_4Br-1	30 mg	300 W Xe lamp	CO	107.1	*Nat. Commun.* **2019**, 10, 2840
$Bi_{12}O_{17}Br_2$ nanotubes	30 mg	300 W Xe lamp	CO	28.3	*ACS Materials Lett.* **2020**, 2, 1025-1032
Sn-BiOBr/$BiOIO_3$	20 mg	300 W Xe lamp	CO	7.4	*Appl. Catal. B Environ.* **2021**, 298, 120618
$BiOIO_3$	20 mg	300 W Xe lamp	CO	2.09	*Appl. Catal. B Environ.* **2021**, 298, 120618
$BiOIO_3$-LOV2	20 mg	300 W Xe lamp	CO	17.33	*Adv. Mater.* **2020**, 32, 1908350
$BiOIO_3$-b3	50 mg	300 W Xe lamp	CO	5.42	*Adv. Funct. Mater.* **2018**, 28, 1804284
5 wt% CPDs/$PbBiO_2Br$	100 mg	300 W Xe lamp	CO	8.28	*Appl. Catal. B Environ.* **2019,** 254, 551-559
ROV $PbBiO_2Br$	20 mg	300 W Xe lamp	CO	4.58	*Appl. Catal. B Environ.* **2020**, 277, 119170

Table S2. Adsorption free energy (E/eV) correction and Gibbs free energy (G/eV) of CO_2 photoreduction to CO for species of BOC (001) and BOC (110).

BOC (001)	**Slab (*)**	***CO_2**	***COOH**	***CO**	**CO**
E/eV	-90.51	-113.70	-115.93	-105.63	/
ΔE/eV	0.00	-0.21	1.15	-0.54	0.33
G/eV	0.00	0.34	1.28	-0.77	-0.22
ΔG/eV	0.00	0.34	1.63	0.86	0.64
BOC (110)	**Slab (*)**	***CO_2**	***COOH**	***CO**	**CO**
E/eV	-57.28	-80.37	-81.61	-72.20	/
ΔE/eV	0.00	-0.11	2.14	-1.42	0.13
G/eV	0.00	0.44	2.27	-1.66	-0.42
ΔG/eV	0.00	0.44	2.72	1.06	0.64